JAMES | Journal of Advances in Modeling Earth Systems

RESEARCH ARTICLE
10.1029/2018MS001492

The Sensitivity of the Jet Stream Response to Climate Change to Radiative Assumptions

Zhihong Tan[1], Orli Lachmy[2], and Tiffany A. Shaw[1]

[1]Department of the Geophysical Sciences, University of Chicago, Chicago, IL, USA, [2]Department of Natural Sciences, Open University of Israel, Ra'anana, Israel

Key Points:
- A new radiation climate model hierarchy is used to examine the impact of radiation on jet stream response to warming
- Gray radiation leads to equatorward shift, but adding four bands and interactive water vapor leads to agreement with comprehensive radiation
- Equatorward and poleward jet shifts are linked to increased poleward wave propagation and increased eddy length scale, respectively

Correspondence to:
Z. Tan,
tanzh@uchicago.edu

Citation:
Tan, Z., Lachmy, O., & Shaw, T. A. (2019). The sensitivity of the jet stream response to climate change to radiative assumptions. *Journal of Advances in Modeling Earth Systems*, *11*, 934–956. https://doi.org/10.1029/2018MS001492

Received 4 SEP 2018
Accepted 16 MAR 2019
Accepted article online 19 MAR 2019
Published online 12 APR 2019

Abstract Comprehensive climate models exhibit a large spread in the magnitude of projected poleward eddy-driven jet shift in response to warming. The spread has been connected to the radiative response to warming. To understand how different radiative assumptions alone affect the jet shift in response to warming, we introduce a new clear-sky longwave radiation hierarchy that spans idealized (gray versus four bands; without or with interactive water vapor) through comprehensive (correlated-k) radiation in the same general circulation model. The new hierarchy is used in an aquaplanet configuration to explore the impact of radiation on the jet stream response to warming, independent of mean surface temperature and meridional surface temperature gradient responses. The gray radiation scheme produces a split jet and its eddy-driven jet shifts equatorward as climate warms, whereas the storm track shifts equatorward then poleward. Including four longwave bands leads to a merged jet that shifts slightly poleward with warming, and the storm track shifts monotonically poleward. Including interactive water vapor makes the poleward jet shift comparable to the jet shift with comprehensive radiation and interactive water vapor. These jet and storm track differences are linked to the radiation response of the stratospheric temperature, the tropopause height, and the meridional gradient of the radiative forcing to warming. Dynamically, the equatorward jet shift with the gray scheme is consistent with reduced wave reflection on the poleward flank of the jet, whereas the poleward jet shift with the other schemes is consistent with increased eddy length scale that favors equatorward wave propagation.

1. Introduction

Jet streams and storm tracks dominate the extratropical circulation. Understanding their responses to climate change is one of the grand challenges of climate science (Bony et al., 2015; Shaw et al., 2016). Comprehensive climate models generally predict the annual mean, zonal-mean eddy-driven jets (indicated by the maximum surface westerlies), and storm tracks shift poleward as climate warms (Barnes & Polvani, 2013; Chang et al., 2012; Manabe & Wetherald, 1975; Shaw et al., 2016; Vallis et al., 2015; Yin, 2005). However, there is significant spread in the climatological jet position and the magnitude of predicted jet shift among climate models, and the theoretical understanding of jet shift is incomplete (Vallis et al., 2015). A similar spread in the jet climatological position and the magnitude of jet shift in response to warming is also found among aquaplanet models (Medeiros et al., 2015).

Recent research has highlighted the importance of the radiative response to climate change, including the role of clouds and water vapor, for the circulation response (Ceppi & Hartmann, 2016; Voigt & Shaw, 2015, 2016). In the literature different jet responses to climate change have also been reported for clear-sky conditions. For example, the jet stream shifts equatorward (Dwyer & O'Gorman, 2017; Schneider et al., 2010) as climate warms in the Geophysical Fluid Dynamics Laboratory (GFDL) gray radiation idealized moist general circulation model, GCM (GRaM, Frierson, 2007; Frierson et al., 2006), opposite to the shift in comprehensive climate models. Interestingly, the storm track position, defined by the maximum near-surface eddy kinetic energy (EKE) (Schneider et al., 2010), by the maximum lower tropospheric poleward eddy heat flux (Dwyer & O'Gorman, 2017), or by the maximum vertically integrated meridional eddy dry static energy (DSE) flux (Lachmy & Shaw, 2018), shifts poleward in GRaM in response to warming. Understanding why these discrepancies arise is important because idealized GCMs with simplified parameterizations like GRaM are used extensively to study the circulation response to climate change.

An important difference between GRaM and the CMIP5 models is their assumptions about radiative transfer. CMIP5 models employ sophisticated radiation schemes with realistic (but approximate) representations of gases, clouds, and aerosols (Li et al., 2013), such as the Rapid Radiative Transfer Model for GCM Applications (RRTMG) scheme (Iacono et al., 2008). In contrast, GRaM utilizes a highly simplified two-stream gray radiation scheme, in which all radiatively active gases are simply approximated as gray absorbers, whose optical depths are prescribed as simple functions of pressure and latitude (Frierson et al., 2006; O'Gorman & Schneider, 2008b). Furthermore, GRaM does not include the radiative feedbacks of water vapor.

An important question is what level of complexity of radiation is needed when simulating the response to climate change? Here we address this question in the context of the jet stream and storm track response to warming. We design a clear-sky longwave (LW) radiation hierarchy including (1) gray radiation, (2) four LW band scheme, (3) four LW band with interactive water vapor, and (4) comprehensive radiative transfer (RRTMG), and examine their responses to warming. The hierarchy is implemented in a slab ocean aquaplanet GCM. Unlike the CMIP5 aquaplanet model intercomparison (Medeiros et al., 2015), we do not prescribe the sea surface temperature (SST) because the surface energy budget is not closed when SSTs are prescribed. Instead, we carefully tune the radiative parameters in the gray and four LW band schemes, so that their respective slab ocean GCMs produce global-mean SSTs and equator-to-pole SST contrasts (subject to closed energy budgets) that are as similar as possible to the RRTMG climatology. The different jet and storm track responses can thus be attributed to the radiative assumptions, rather than differences in SSTs. This approach is complementary to Lu et al. (2010), who varied the SST distribution but kept the radiation scheme unchanged to investigate the SST-driven jet and storm track responses. Our radiation hierarchy complements other idealized modeling frameworks called MiMA and Isca (Jucker & Gerber, 2017; Vallis et al., 2018). MiMA and Isca use a different radiation hierarchy (two LW bands with interactive water vapor and RRTMG) and does not include parameter tuning to match a reference climate.

The paper is structured as follows: Section 2 describes the configuration of the aquaplanet GCM and the hierarchy of radiation schemes; section 3 compares the simulated climatological temperature, radiative cooling profiles, and zonal-mean zonal wind for the different radiation schemes; section 4 compares the temperature and zonal-mean zonal wind responses to warming for the different radiation schemes; section 5 analyzes the dynamical mechanisms of the jet shifts; section 6 summarizes the conclusions.

2. Method

2.1. Aquaplanet GCM

We use an aquaplanet GCM with the finite-volume dynamical core of the GFDL AM2.1 model (GFDL-GAMDT, 2004; Delworth et al., 2006; Lin, 2004). The nonradiation physical parameterizations (turbulence, convection, and precipitation) are as in Frierson et al. (2006), Frierson (2007), and O'Gorman and Schneider (2008a). More specifically, the idealized GCM parameterization includes a Monin-Obukhov similarity scheme for the surface fluxes, a k-profile diffusivity scheme for the vertical turbulent transport in the boundary layer, a simplified Betts-Miller scheme for quasi-equilibrium moist convection, and a saturation adjustment scheme for grid-scale precipitation.

Following Kang et al. (2008), the aquaplanet includes a slab ocean with a mixed layer depth of 30 m. There is no ocean heat transport or sea ice, and the seasonal and diurnal cycles of insolation are disabled for simplicity (see section 2.3). One consequence of having zero ocean energy transport is that the Hadley circulation is stronger than its real world counterpart because of missing ocean energy transport (Merlis & Schneider, 2011). The GCM is configured at a uniform horizontal resolution of 2.8° (i.e., ~300 km at the equator), which is comparable to the T42 resolution of a spectral GCM (O'Gorman & Schneider, 2008a); Frierson et al. (2006) reported that the midlatitudes simulated by a similar aquaplanet GCM were insensitive to further refinements of horizontal resolution. The model is run with 48 unevenly spaced vertical σ-levels (with 18 levels below $\sigma = 0.7$, and 13 levels above $\sigma = 0.1$). For numerical stability, the four top levels (above $\sigma = 0.006$) are configured as sponge layers where diffusion is enhanced using a first-order upwind horizontal advection scheme, and a Rayleigh drag with a 40-day time scale is applied to the full momentum at the topmost level (above $\sigma = 0.002$). The model time step is 900 s. The simulations are first spun up for 10 years (without interactive water vapor radiative effects) or 20 years (with interactive water vapor radiative effects), and the output data are averaged over the next 10 years and over both hemispheres.

2.2. Longwave Radiation Hierarchy

We design a clear-sky LW radiation hierarchy that includes the gray radiation scheme (GR), the four LW band scheme without interactive water vapor (FB) or with interactive water vapor (WV), and the RRTMG scheme. The parameters of GR, FB, and WV are tuned to match the global-mean SST and equator-to-pole SST contrast of RRTMG as closely as possible. The LW effects of clouds and the ozone layer are also excluded from the LW hierarchy.

2.2.1. Gray Scheme

The GR scheme follows the formulation by Frierson et al. (2006) and O'Gorman and Schneider (2008a), whose LW optical depth τ_0 depends on latitude ϕ and pressure p as follows:

$$\tau_0 = \left[f_l \frac{p}{p_s} + (1 - f_l)\left(\frac{p}{p_s}\right)^4 \right] \tau_T; \quad \tau_T = \tau_e + (\tau_p - \tau_e)\sin^2\phi, \tag{1}$$

where p_s is the surface pressure, f_l is the linear absorption factor, and τ_T is the surface LW optical depth as a function of ϕ (it equals τ_p at the poles and τ_e at the equator). The linear term with factor f_l mimics the well-mixed greenhouse gases (GHG; dominant in the upper troposphere and stratosphere), and the quartic term with factor $(1 - f_l)$ mimics the water vapor (dominant in the lower troposphere) based on the approximation that the water vapor density scale height is roughly one quarter of the total density scale height (Frierson et al., 2006). This formula thus represents a linear dependence of optical depth on the absorber mass. The pressure broadening effect is not included (cf. Beucler & Cronin, 2016).

We set $f_l = 0.20$ following O'Gorman and Schneider (2008a) and tune the two remaining parameters (τ_p, τ_e) to match the global mean and the pole-to-equator contrast of SST in the RRTMG control climate. The tuning is unique because there are exactly two constraints and two unknowns, and the result is $(\tau_p, \tau_e) = (3.13, 5.40)$. We simulate climate change by multiplying τ_T with a scaling factor α from 0.43 to 3.30, which reproduces the global-mean SST response for RRTMG as CO_2 increases from 0.001 times to 32 times the control concentration (see section 2.2.4).

2.2.2. Four-Band Scheme

The GR scheme has a single LW band, and its LW cooling profile is too shallow and concentrated in the middle troposphere, where the LW optical depth is about one (see section 3.3). It also fails to produce the robust stratospheric cooling trend in RRTMG (see section 4.2). With multiple LW bands, the radiative cooling deepens and becomes more homogeneous because each band cools preferentially around its emission height. The stratosphere cooling trend is also recovered, because the stratospheric temperature is set by the thickest LW band whose emission temperature decreases as SST warms (see Appendix A).

We increased complexity by including four equal-width LW bands, which is sufficient to eliminate the qualitative differences compared to RRTMG. Including only two or three LW bands also leads to deepened radiative cooling and reproduces much of the temperature and zonal wind climatology and responses as in RRTMG (not shown), but the vertical profile of radiative cooling is not sufficiently smooth because the cooling maximum of each band is too distinctive. Further increasing the number of LW bands beyond four bands or using unequal widths does not lead to significant improvement.

The four bands are not intended to represent actual spectral features such as individual GHG or frequency bands. Instead, they represent a simplified view of the nongray LW effects based on an idealized binning of the entire LW spectrum by optical depth (and correspondingly the emission height). The optical depth parameters are empirically tuned to roughly match the vertical structure of LW cooling by RRTMG; however, quantitative agreements to comprehensive radiation are not expected. As a natural extension of the gray scheme, the four-band scheme retains most of its formal simplicity, which facilitates our physical understanding of the nongray LW effects (e.g., Appendix A) and is easier to perturb in a controlled manner.

We prescribe the LW optical depth τ_i for each band i as $\tau_i = \beta_i \tau_0$, with τ_0 given by equation (1) and β_i as a scaling constant. The height of maximum LW cooling for each band occurs where $\tau_i \sim O(1)$, roughly corresponding to the height where $4\log(p/p_s) \sim \log(\beta_i \tau_T)$, assuming that the quartic term dominates in equation (1). Therefore, we choose β_i as a geometric series, that is, $[\beta_1, \beta_2, \beta_3, \beta_4] = \beta_0^{[3,1,-1,-3]}$ with $\beta_0 \geq 1$, so that the maximum LW cooling for each band is roughly evenly spaced in height (i.e., in $\log p$). The choice of β_0 controls the vertical structure of LW cooling: a larger β_0 leads to more distinct emission heights and a broader cooling profile, but the vertically integrated atmospheric LW cooling is weaker. We set $\beta_0 = 20^{1/3}$ so that the total atmospheric LW cooling roughly matches that of RRTMG.

Additionally, f_l is reduced to 0.01 to limit the stratospheric LW cooling efficiency and to better match the stratospheric temperature pattern in RRTMG (see section 3.2). Following the tuning outlined for the GR scheme, (τ_p, τ_e) are set as (4.21, 15.23) to match the SST in control RRTMG. We simulate climate change by multiplying τ_T with a scaling factor α from 0.20 to 8.40, which reproduces the global-mean SST response for RRTMG as CO_2 increases from 0.001 times to 32 times the control concentration (see section 2.2.4).

2.2.3. Four Band With Interactive Water Vapor

The sine-latitude formulation of LW optical depth in FB does not capture the enhanced LW optical depth associated with water vapor in the deep tropics compared to the drier subtropics, and it does not sufficiently capture the increased meridional contrast in the LW water vapor feedback between the tropics-subtropics and extratropics as climate warms, since its LW optical depth is scaled up by a uniform factor across all latitudes. This leads to differences in the climatology and response of the meridional profile of top of atmosphere (TOA) energy budget. By including a simple representation of the water vapor LW effect, the meridional contrasts of LW optical depth are largely reproduced and the TOA energy budget is closer to RRTMG (see section 3.1).

We increased complexity by adding the radiative effect of water vapor. The LW optical depth for each band is formulated as

$$\tau_i = \beta_i \left[\tau_D \frac{p}{p_s} + p_w^{-1} \int_0^p q \mathrm{d}p \right], \tag{2}$$

where the first and second terms represent the LW effects of well-mixed dry GHG and spatially inhomogeneous water vapor, respectively. The parameter τ_D is the horizontally uniform dry optical depth, p_w represents the column water vapor pressure corresponding to unit optical depth, q is the specific humidity (taken from the instantaneous model output), and the values of β_i are set exactly the same as FB.

Initially, we follow Byrne and O'Gorman (2012) and tune the parameters (τ_D, p_w) to match the control FB vertical profile of average LW optical depth between 20 and 40° latitudes; the fit values are $\tau_D = 1.82$ and $p_w = 10^5/5126.9 \approx 20$ Pa. However, this τ_D turns out much too large and leads to a very warm climate. Therefore, we keep $p_w = 20$ Pa, but reduce τ_D to 0.38 to match the global-mean SST of control RRTMG. Unlike GR and FB, the pole-to-equator SST contrast in WV cannot be matched exactly to RRTMG: it is only weakly sensitive to p_w (see section 3.1) and there are no additional tuning parameters. The value of τ_D is still larger than the linear absorption parameters in the FB scheme, which lies between $f_l\tau_p = 0.04$ and $f_l\tau_e = 0.15$. The higher stratospheric LW emissivity leads to quantitative differences in the simulated stratospheric temperature and jet pattern compared to FB (see sections 3.2 and 3.4). We simulate climate change by multiplying τ_D with a scaling factor α from 0.13 to 2.75, which reproduces the global-mean SST response for RRTMG as CO_2 increases from 0.001 times to 32 times the control concentration (see section 2.2.4).

2.2.4. RRTMG

The RRTMG scheme is based on the correlated-k method (Iacono et al., 2008). The well-mixed GHG concentrations in the control climate are prescribed as in Lachmy and Shaw (2018): $CO_2 = 355$ ppmv, $CH_4 = 1700$ ppbv, and $N_2O = 320$ ppbv. The O_3 concentration is 30 ppbv everywhere (including the stratosphere). This O_3 concentration is representative of the lower tropospheric mean (below 500 hPa) in the Aqua-Planet Experiment (Blackburn & Hoskins, 2013), and it is higher than the observed near-surface concentration (~10 ppbv). There are no chlorofluorocarbons, clouds, aerosol or stratospheric ozone layer (apart from the baseline value of 30 ppbv) in the model. Our implementation of the RRTMG scheme is very similar to (but independent of) that in the MiMA and Isca models (Jucker & Gerber, 2017; Vallis et al., 2018), with the only apparent differences being that they use a different default CO_2 concentration, excludes CH_4 and N_2O, and includes an ozone layer. We simulate climate change by perturbing the CO_2 concentration from 0.001 times to 32 times control CO_2 concentration.

2.3. Shortwave Radiation

We focus on the clear-sky shortwave (SW) effects without the ozone layer as in Frierson et al. (2006) and O'Gorman and Schneider (2008a). In reality, the radiative effects of the ozone layer and clouds affect the stratospheric temperature, the tropopause height, and the latitudinally dependent TOA energy budget. These effects will be investigated in a future study.

For a more direct comparison with previous GRaM and CMIP5 studies, we use two clear-sky SW schemes representative of both types of models to accompany their respective LW schemes. The GRaM-type SW

scheme, which is used for all LW schemes except RRTMG, is a simple SW absorption scheme with a uniform surface albedo of 0.38 (O'Gorman & Schneider, 2008a). The CMIP5-type SW scheme is RRTMG (Iacono et al., 2008) that accompanies its LW scheme with the same gas concentrations; this approach is again similar to the MiMA and Isca models (Jucker & Gerber, 2017; Vallis et al., 2018). The RRTMG scheme computes SW absorption using a correlated-k method and a surface albedo of 0.25, which compensates for the lack of clouds, ice, and ozone. We prescribe the insolation S for both SW schemes simply as a time-independent latitude-dependent function:

$$S = \frac{S_0}{4}\left[1 + \frac{\Delta_s}{4}(1 - 3\sin^2\phi)\right], \tag{3}$$

where $S_0 = 1{,}360\ \mathrm{W/m^{-2}}$ is the solar constant and $\Delta_s = 1.2$ is a parameter for pole-to-equator insolation contrast (O'Gorman & Schneider, 2008a). The insolation at the equator and at the poles are respectively $0.325S_0$ and $0.100S_0$; this contrast is smaller than the equinox insolation used by Kang et al. (2008; $0.318S_0$ and 0) but is slightly larger than the annual mean insolation used by Ceppi & Hartmann (2016; $0.305S_0$ and $0.127S_0$).

The resulting SW forcing differs between the two schemes: the TOA albedo is about 0.24 for RRTMG and about 0.30 for the GRaM-type SW scheme. The smaller TOA albedo with RRTMG compensates the larger climatological outgoing longwave radiation (OLR) due to the lack of LW cloud effects. In contrast, although the other LW schemes do not include interactive cloud effects, the global-mean LW cloud effects are implicitly included in the tuning of LW parameters that ensures a realistic OLR (and thus TOA albedo). Since there is no ozone layer in both schemes, the differences in SW forcing are concentrated in the lower troposphere (where the SW heating due to water vapor maximizes in RRTMG), and they are not the main contributors for the jet discrepancies among radiation schemes, which are more closely linked to the differences in LW radiative forcing and thermal structure of the upper troposphere and stratosphere (see section 3.4).

2.4. Radiative-Convective Equilibrium Model

In order to separately quantify the radiative and large-scale dynamical effects on temperature we configure a radiative-convective equilibrium (RCE) model for each radiation scheme. Since the RCE models do not include the changes in water vapor induced by large-scale dynamics, their WV and RRTMG cases do not capture the associated radiative effects as in the GCMs.

The RCE model is exactly the same as the aquaplanet GCM with all its parameterizations, except that the grid-scale advective tendencies of wind, temperature, and specific humidity are disabled (e.g., Haqq-Misra et al., 2011). The wind speed for the surface sensible and latent heat flux calculations is fixed at 7 m/s, which is roughly consistent with the global-mean surface wind speed in the full GCM runs. The results are nearly identical if the zonal-mean surface wind speed is prescribed.

The SST in the RCE model is prescribed. A prescribed SST approach is also used in the radiative-convective equilibrium model intercomparison project (RCEMIP; Wing et al., 2018). However, here a latitudinally dependent SST diagnosed from the time mean zonal-mean SST of the corresponding GCM is used. Therefore, the RCE model results include the GCM large-scale dynamical effects that set the meridional SST pattern, but they do not include the large-scale dynamical effects that impact the vertical structures of temperature and specific humidity (and the associated water vapor radiative effects in WV and RRTMG).

A slab ocean RCE model may also be configured, but its SST pattern is only comparable to the GCM if (1) the energy input to the atmosphere (EIA) in the GCM is prescribed as an ocean cooling term in the RCE model, and (2) the zonal-mean specific humidity in the GCM is prescribed as input to the radiation schemes for WV and RRTMG. Using interactive specific humidity in WV and RRTMG would cause excessive subtropical warming, where the RCE model is moister than GCM due to the lack of subsidence drying (details in Appendix B). Because the specific humidity is partly determined by the large-scale circulation, the slab ocean RCE model provides a less clear separation between the large-scale dynamical and radiative effects and thus is not used for this study.

2.5. Circulation Diagnostics and Spectral Analyses

Following Lachmy and Shaw (2018), we identify the eddy-driven jet as the latitude of maximum surface westerlies (which aligns with the maximum surface zonal wind stress and maximum vertically integrated eddy meridional momentum flux convergence, see Appendix C) and the latitude of maximum vertically

integrated eddy meridional dry static energy (DSE) flux, respectively. This energy-based definition of storm track facilitates the energetic arguments of the storm track responses to warming (Barpanda & Shaw, 2017; Shaw & Voigt, 2016; Shaw et al., 2018). The storm track responses are qualitatively unchanged with alternative metrics based on the vertically integrated eddy heat flux (the dominant component of the eddy DSE flux) or the near-surface EKE (see Appendix C). The DSE flux analysis is performed in the native σ-coordinate of the GCM, and thus the eddies are defined as the deviations from the mass-weighted zonal mean, that is, weighted by surface pressure (Lachmy & Shaw, 2018; O'Gorman & Schneider, 2007); the mass-weighted zonal mean is consistent with the (mass-weighted) vertical integral such that the two operators are commutative. Both metrics are area-weighted by the cosine of latitude and averaged for both hemispheres, and the latitudes of maxima are identified after interpolating the metrics onto a 0.02° latitudinal grid using the spline method. We further estimate the 95% confidence intervals of the metrics by bootstrapping 90-day segments of the 10-year data from both hemispheres ($40 \times 2 = 80$ segments in total) 10,000 times.

In order to understand the mechanisms driving the eddy-driven jet shift in response to warming, we analyze the zonal wave number spectra and the wave number-phase speed cospectra of the eddy streamfunction variance and the eddy momentum flux (EMF). We follow the method by Randel and Held (1991) and first compute the smoothed wave number-time cospectra (we use a simple three-point running average instead of their Gaussian filter), and then convert them into the wave number-phase speed cospectra with total power conserved. We use 90-day segments of 6-hourly output, and we average the cospectra over all segments through the 10-year analysis period and for both hemispheres. The phase speed range is -30 to 30 m/s^{-1} with an interval of 0.5 m/s. The statistical significance of the spectral responses to warming is tested at each latitude and wave number (or phase speed) by performing a Welch's t test on the 90-day segment data at a significance level of 0.05; the results are similar with a Kolmogorov-Smirnov test (not shown).

We limit the wave number-phase speed cospectra analyses to a single level in the upper troposphere ($\sigma = 0.245$), which is representative of the control climate and the responses of total EMF. In order to test explanations of the jet shift based on barotropic arguments, we define the phase speed $c_{r,k}$ of the reflecting level corresponding to zonal wave number k as its minimum allowable Rossby wave phase speed, which corresponds to zero meridional wave number:

$$c_{r,k} = \bar{u} - k^{-2}\beta^*(a\cos\phi)^2, \tag{4}$$

where $\bar{u}$ is the zonal-mean zonal wind, f is the Coriolis parameter, a is Earth's radius, ϕ is the latitude, and $\beta^* = \partial_y f - \partial_{yy}\bar{u}$ is the absolute vorticity gradient. Note that β^* differs from the absolute potential vorticity gradient in that it excludes the stretching term, as is consistent with the barotropic assumption. The reflecting phase speed $c_{r,k}$ also corresponds to minimum phase speed at the limit of refractive index $n = 0$ for the barotropic Rossby wave (O'Rourke & Vallis, 2013). In practice, $c_{r,k}$ is computed with time mean $\bar{u}$ (instead of the instantaneous $\bar{u}$).

3. Control Climate

In this section, we compare the control climates across the radiation hierarchy, and we discuss how the climatological differences in temperature, radiative cooling tendency, and zonal wind are linked to the different radiative assumptions. This sets the stage for the subsequent section which assesses the impact of radiative assumption on the jet stream and storm track responses to warming.

3.1. SST and EIA

Since the radiation parameters are carefully calibrated, the meridional SST distributions are almost identical between the GR, FB, and RRTMG schemes, and their global-mean SSTs are very close to 288 K (Figure 1, top left panel). However, the equator-to-pole SST contrast (0–10° minus 70–90°) is about 10 K higher in WV. This is related to its linear dependence of LW optical depth on both dry and water vapor air masses (section 2.2.3): the polar LW optical depth is small and its vertical profile is nearly linear, which is favorable for LW cooling at the surface and a low polar SST; additional tuning did not reduce the SST contrast. The free tropospheric equator-to-pole temperature contrast in WV is still comparable to the other schemes (Figure 1, top right panel). Prescribing the RRTMG SSTs in the GCMs with GR, FB, and WV radiation schemes shows that the vertical structures of temperature and zonal wind are almost unaffected by their SST biases (see Appendix D).

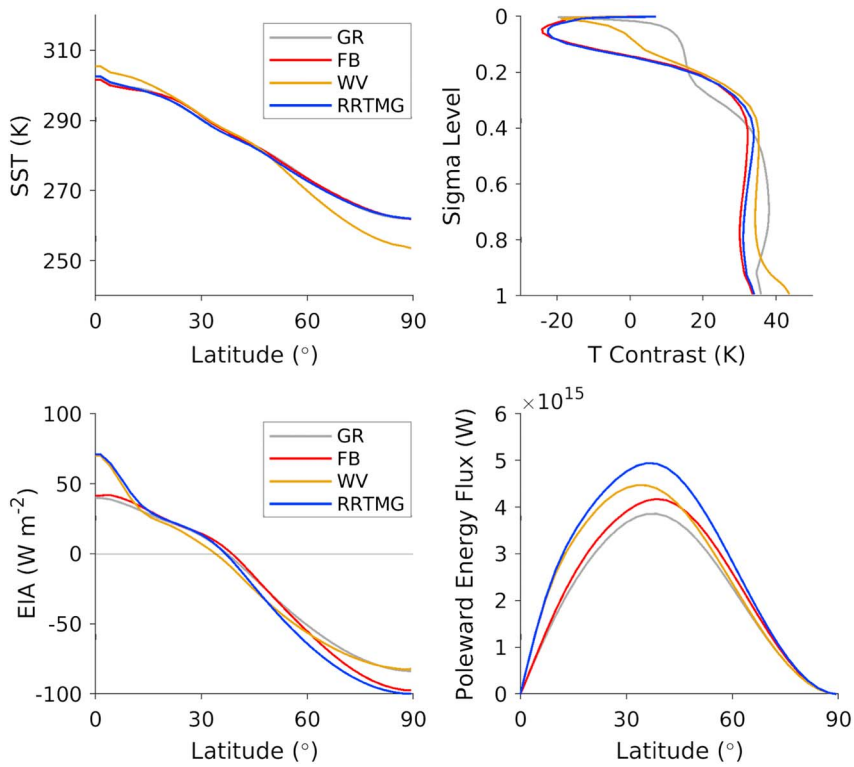

Figure 1. (top left) Sea surface temperature (SST) as a function of latitude, (top right) vertical profile of zonal-mean equator-to-pole temperature contrast (0–10° minus 70–90°), (bottom left) energy input to the atmosphere as a function of latitude, and (bottom right) poleward energy transport as a function of latitude, for the control climate.
EIA = energy input to the atmosphere; GR = gray radiation scheme; FB = four longwave-band scheme; WV = four longwave band with interactive water vapor; RRTMG = Rapid Radiative Transfer Model for GCM; GCM = general circulation model.

The interactive water vapor has a significant effect on the climatological EIA (Figure 1, bottom left panel). In WV and RRTMG, the water vapor feedback reduces the OLR in the tropics (0–15°) compared to the subtropics (15–35°), leading to a larger EIA in the tropics. In reality, the EIA around the Intertropical Convergence Zone is reduced by cloud shortwave effects, but the overall tropical-subtropical EIA contrast is still comparable to our WV and RRTMG cases (Stephens & L'Ecuyer, 2015, Figure 5b). The maximum poleward energy transport is correspondingly larger in WV and RRTMG than in GR and FB (Figure 1, bottom-right panel).

3.2. Temperature Structure and Tropopause

The tropopause is defined as the lowest level at which the lapse rate decreases to 2 K/km or less, provided that the average lapse rate between this level and all higher levels within 2 km does not exceed 2 K/km (Reichler et al., 2003). The inclusion of four LW bands leads to a much higher and colder tropical tropopause in FB and WV ($p \approx 60$ hPa and $T \approx 180$ K) than in GR ($p \approx 200$ hPa and $T \approx 230$ K; magenta lines, Figure 2). The FB and WV tropopause is close to that of RRTMG and is consistent with the no-ozone results of Manabe and Strickler (1964). The vertical temperature structure of FB and WV is also closer to RRTMG than GR (Figure 2, top row, gray lines). Clearly, the choice of radiation scheme has a large impact on the climatological temperature structure.

We use the RCE model to separate the radiative and dynamical effects on the vertical temperature structure. In the tropics, the GCM climatological zonal-mean temperature and tropopause are reasonably well reproduced by the RCE model (Figure 2, bottom row, gray lines). This indicates that the warm and low tropical tropopause in GR is a direct consequence of its radiative assumption. It is further demonstrated in Appendix A1 that the warm GR stratosphere originates from its assumption of a single gray LW band, and it can only be resolved by adding more LW bands (as with FB and WV).

Some aspects of the temperature structure are dynamical and are not captured by the RCE models. For example, the extratropical stratification is much weaker and the meridional temperature gradient in the

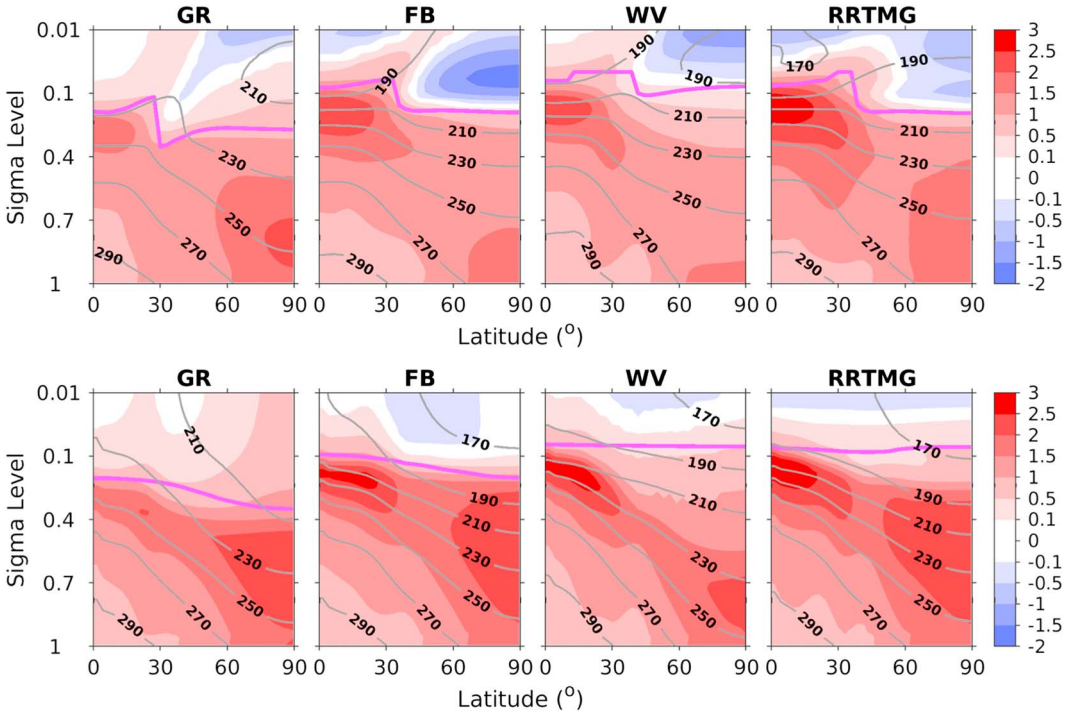

Figure 2. Zonal-mean temperature for the control climate (gray lines, unit is K) and the response to warming normalized by the global-mean sea surface temperature increase (shading, unit is K/K). The response to warming is defined as the difference between the representative warm and control climates with global-mean sea surface temperatures of 300 K and 288 K, respectively. (top row) GCMs; (bottom row) radiative-convective equilibrium models. (first column) GR = gray radiation scheme; (second column) FB = four longwave-band scheme; (third column) WV = four longwave band with interactive water vapor scheme; (fourth column) RRTMG = Rapid Radiative Transfer Model for GCM. The γ axis is linear below $\sigma = 0.1$ and logarithmic above $\sigma = 0.1$. The magenta line indicates the climatological tropopause. GCM = general circulation model.

midtroposphere is much larger in the RCE models due to the lack of baroclinic eddies. The stratospheric meridional temperature gradient is also reduced (or slightly reversed) in GCMs by the stratospheric poleward eddy heat flux; in the transformed Eulerian mean (TEM) framework this corresponds to a residual circulation with tropical upwelling and extratropical downwelling. This dynamical effect is most significant for FB and RRTMG (Figure 2, the second and fourth columns of the top row): since their stratospheric LW emissivities are weak, the LW cooling is inefficient to reestablish the RCE temperature gradient (section 2.2.2 and Appendix A3). The sharp jump between the tropical and extratropical tropopause is also dynamical.

3.3. Radiative Tendency

To better understand how the different radiation schemes produce different EIA and tropopause heights, we compare the total (LW + SW) radiative tendencies (Figure 3). For all schemes, the radiative tendencies are dominated by LW cooling at most levels. The GR scheme concentrates radiative cooling around $\sigma = 0.6$, and in the tropics the cooling does not extend above $\sigma = 0.3$. In contrast, all other schemes have multiple LW bands, and they produce LW cooling across a deeper layer, because the LW bands have different optical depths and cool at different heights. Consequently, radiative cooling is more vertically uniform (except in the deep tropics of WV), and the tropical cooling extends higher than $\sigma = 0.2$. The vertical structure of GR radiative cooling is consistent with its much lower tropopause (Figure 2, top row).

Because of the water vapor-induced contrast in LW opacity, the schemes with interactive water vapor (WV and RRTMG) produce a sharper meridional contrast in LW cooling: in the upper troposphere ($\sigma < 0.4$), the LW cooling is stronger in the tropics than subtropics, whereas the contrast is reversed in the lower troposphere ($\sigma > 0.7$). Consequently, WV and RRTMG display larger tropical-subtropical contrasts in the bulk LW emission height (the height where temperature equals the bulk emission temperature, cyan lines in Figure 3), which is consistent with the lower OLR and the larger EIA in the tropics (Figure 1, bottom left panel). This tropical-subtropical contrast in the radiative cooling structure, LW emission height, and EIA is less pronounced in GR and FB.

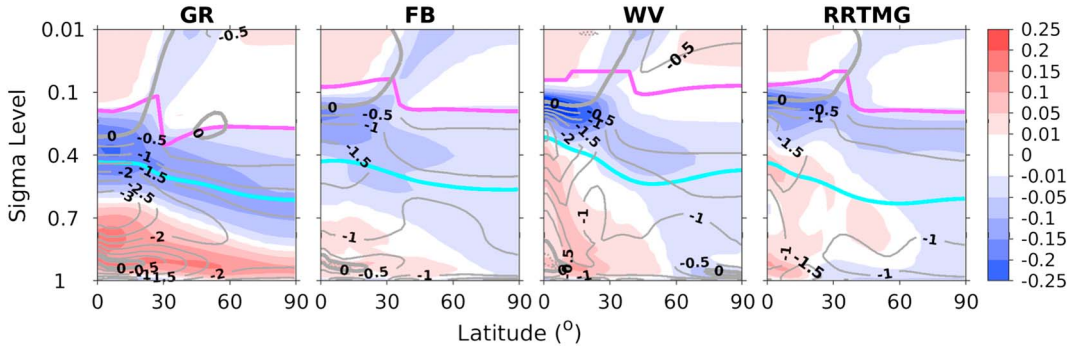

Figure 3. Net radiative heating rate (longwave + shortwave) for the control climate (lines, unit is K/day) and its response to warming normalized by global-mean sea surface temperature increase (shading, unit is $K{\cdot}day^{-1}{\cdot}K^{-1}$). From left to right, (first panel) GR = gray radiation scheme; (second panel) FB = four longwave-band scheme; (third panel) WV = four longwave band with interactive water vapor scheme; (fourth panel) RRTMG = Rapid Radiative Transfer Model for GCM. The solid and dotted lines indicate cooling and heating tendencies, respectively; the thick gray line indicates zero radiative tendency; the thick cyan line indicates the bulk longwave emission height; the magenta line indicates the climatological tropopause. GCM = general circulation model.

The stratospheric radiative heating in the tropics and radiative cooling in the extratropics (separated by the thick gray lines in Figure 3) are robust across all schemes. These radiative tendencies act to oppose and balance the tendencies produced by stratospheric dynamics (section 3.2). For GR, FB, and WV cases, the net radiative warming around the tropical lifting condensation level ($\sigma \approx 0.9$) corresponds to a concave point in the vertical temperature profile (i.e., a local maximum of $\partial^2 T/\partial z^2$) caused by the transition from dry to moist lapse rate; this tropical lower tropospheric net radiative warming also occurs in the warm RRTMG case (not shown).

3.4. Zonal Wind

The different temperature structures seen for the different radiation schemes are connected to the zonal wind via thermal wind balance. The GR control climate has a low tropical tropopause and a relatively strong stratospheric meridional temperature gradient. This corresponds with a split jet pattern consisting of a weak subtropical jet (since the thermal wind relation is integrated over a shallower troposphere) and a strong stratospheric polar vortex (Figure 4, left panel). The maximum surface westerlies occur at about 49° latitude. For the control climates of the other schemes, the tropical tropopause is much higher and consistently the subtropical jet is deeper and stronger and merged with the eddy-driven jet (Figure 4, three right panels). The maximum surface westerlies occur much further equatorward (at about 36° latitude) than for GR, and weak

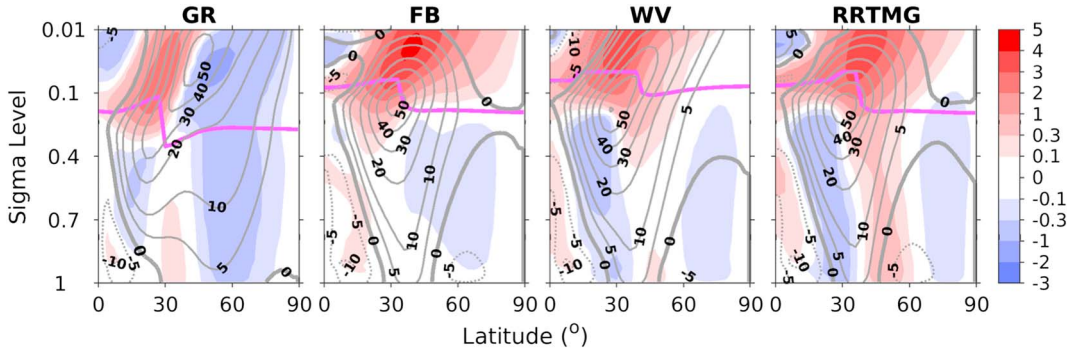

Figure 4. Zonal-mean zonal wind for the control climate (lines, unit is m/s, dotted for negative values, thick gray line for zero wind) and its response to warming normalized by global-mean sea surface temperature increase (shading, unit is $m{\cdot}s^{-1}{\cdot}K^{-1}$). From left to right, (first panel) GR = gray radiation scheme; (second panel) FB = four longwave-band scheme; (third panel) WV = four longwave band with interactive water vapor scheme; (fourth panel) RRTMG = Rapid Radiative Transfer Model for GCM. The magenta line indicates the climatological tropopause. GCM = general circulation model.

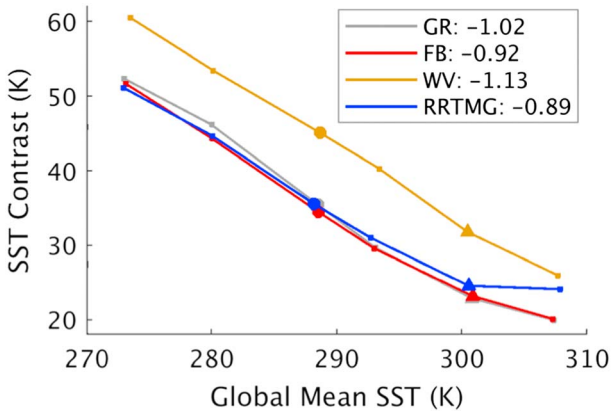

Figure 5. The equator-to-pole SST contrast (0–10° minus 70–90°) versus the global-mean SST in the climate change experiments. The large circles represent the control climates (288 K); the large triangles indicate the representative warm climates (300 K), and the values in the legends indicate SST contrast changes from control to warm climates normalized by global-mean SST increase (unit is K/K). GR = gray radiation scheme; FB = four longwave-band scheme; WV = four longwave band with interactive water vapor scheme; RRTMG = Rapid Radiative Transfer Model for GCM; GCM = general circulation model; SST = sea surface temperature.

easterlies prevail in the polar stratosphere. There is no stratospheric polar vortex for FB and RRTMG, which is consistent with their stratosphere being slightly warmer at the poles than the midlatitudes (Section 3.2).

4. Response to Warming

Various thermodynamic responses are expected to occur as climate warms, such as increased tropical stability, rise in the tropopause height, increased pole-to-equator contrast of near-surface moist static energy, and increased poleward atmospheric energy transport; these responses are energetically and dynamically connected to the jet and storm track responses (Barpanda & Shaw, 2017; Shaw & Tan, 2018; Shaw & Voigt, 2016; Vallis et al., 2015). The magnitude of these thermodynamic responses are sensitive to radiative assumptions. Here we compare the temperature, poleward energy transport, jet and storm track responses across the radiation hierarchy, and we discuss how radiative assumptions affect these differences. The dynamical mechanisms of the jet responses will be discussed in section 5.

4.1. SST and EIA

We begin by examining the equator-to-pole SST contrast as a function of global-mean SST (Figure 5). As the climate warms, the SST contrast is reduced by about 1 K per 1 K increase of global-mean SST with all schemes. The global-mean SST ranges from 273 to 308 K. The equator-to-pole contrast ranges from 20 to 50 K with a larger value in the WV scheme.

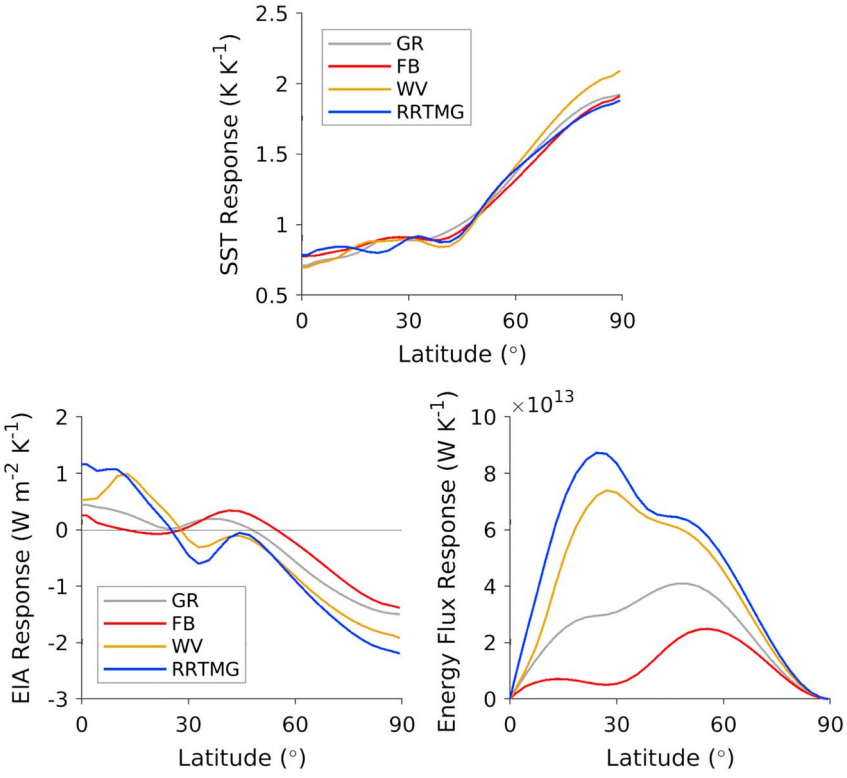

Figure 6. The response of (top) SST, (bottom left) energy input to the atmosphere, and (bottom right) poleward energy transport to warming, normalized by the global-mean SST increase. GR = gray radiation scheme; FB = four longwave-band scheme; WV = four longwave band with interactive water vapor scheme; RRTMG = Rapid Radiative Transfer Model for GCM; GCM = general circulation model; SST = sea surface temperature.

In what follows, climate change is defined as the difference between the representative warm climates (global-mean SST of 300 K, the cases with triangle signs in Figure 5) and control climates. The warm climates correspond to 16 times the control CO_2 concentrations with RRTMG, and LW optical depth factors of $\alpha = 2.1$ with GR, $\alpha = 3.8$ with FB, and $\alpha = 2.0$ with WV.

The latitudinal structure of the SST responses as climate warms is very similar for all radiation schemes (Figure 6, top panel): per 1 K of global-mean SST increase, the tropical and subtropical (0–35°) SST increases by 0.7–0.9 K, whereas the polar (70–90°) SST increases by 1.6–2.0 K. The similarity of the SST responses indicates that the different circulation responses between the radiation schemes (to be discussed in section 4.3) are mostly SST independent.

In contrast, the meridional distribution of EIA responses differs between the schemes with interactive water vapor (WV and RRTMG) and those without (GR and FB). In WV and RRTMG, the clear-sky water vapor feedback enhances the EIA increase in the tropics and most of the subtropics (0–30°, where water vapor increases the most) and the EIA decrease in the extratropics (Figure 6, bottom left panel). The larger tropical-subtropical energy surplus must be balanced by a larger increase in the poleward atmospheric energy flux (Figure 6, bottom right panel). In GR and FB, the climate warming is produced by scaling up the LW optical depths uniformly (sections 2.2.1 and 2.2.2), which does not fully capture the latitudinal contrast in the water vapor feedback and leads to a smaller latitudinal contrast in EIA response and smaller atmospheric energy flux response.

4.2. Temperature Structure

In response to warming, all of the radiation schemes produce qualitatively similar temperature responses, including amplified warming aloft in the tropics and most of the subtropics, and amplified warming at the poles at the surface (Figure 2, top row, shading). However, the heating due to the tropical lapse rate feedback is too low and too weak with GR, since its climatological tropopause is too low. It also fails to reproduce the global-mean stratospheric cooling seen with FB and RRTMG (and with WV but limited to higher altitudes). In contrast, all the other schemes produce a robust increase in the upper tropospheric temperature gradient due to the upper tropospheric warming and lower stratospheric cooling, which is consistent with CMIP5 models (Vallis et al., 2015).

As LW opacity increases, the patterns of tropospheric radiative tendencies migrate upward (Figure 3, shading), consistent with the upward shift of the vertical structure of the atmosphere (Singh & O'Gorman, 2012). For GR and FB, the tropical radiative cooling is enhanced above the lower troposhere ($\sigma < 0.7$). This differs from WV and RRTMG, for which the tropical radiative cooling is only enhanced in the upper troposphere ($\sigma < 0.4$) but reduced in the middle to lower troposphere. This is consistent with the tropical-enhanced increase in the LW opacity and EIA by the water vapor feedback in WV and RRTMG. For all schemes, the heating-cooling dipole of the stratospheric radiative tendencies is enhanced slightly in the tropics and midlatitudes, which counteracts the enhanced dynamical cooling-heating dipole by the strengthened stratospheric residual circulation (not shown). The radiative tendency changes little in the polar lower stratosphere.

We again use the RCE model with prescribed SST to separate the radiative-convective contributions from the large-scale dynamical contributions. The amplified warming of the tropical upper troposphere is reasonably well captured by the RCE model, which is consistent with the lapse rate feedback due to moist adiabatic adjustment (Figure 2, bottom row, shading). However, the lapse rate feedback occurs beyond the tropics, because convection is ubiquitous in the RCE model. The polar amplification is also spread by convection to a deeper layer than in the presence of the large-scale circulation.

The comparison of RCE and GCM temperature responses also suggests the differences in the global-mean stratospheric temperature responses are largely radiation induced. The lack of stratospheric cooling in GR is a consequence of its assumption of a single LW band, which keeps its global-mean TOA temperature fixed; adding more LW bands generally leads to a cooling response of TOA temperature due to the OLR compensation between thick and thin bands (details in section A2). This is demonstrated by the stratospheric cooling response in the FB RCE model as climate warms, which is weaker than that in RRTMG. The stratosphere for WV cools less strongly than FB and RRTMG because of its larger stratospheric emissivity and stronger greenhouse warming (see sections 2.2.3 and A3).

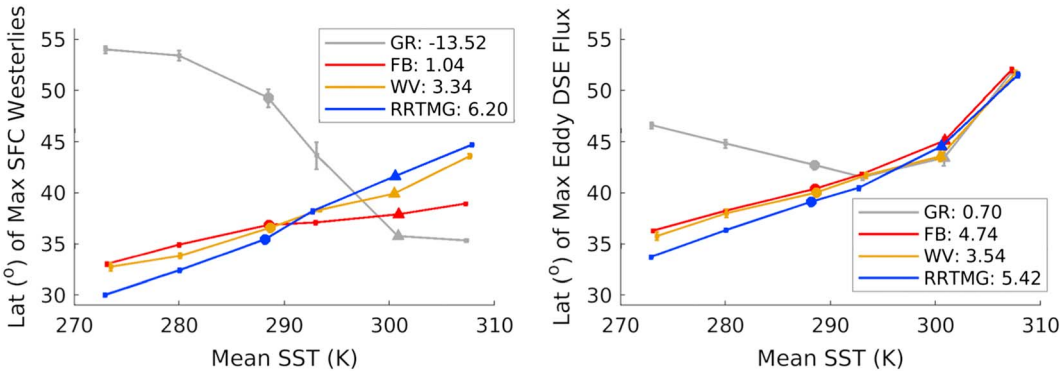

Figure 7. The latitudes of maximum (left) surface westerlies and (right) vertically integrated poleward eddy dry static energy flux versus the global-mean SST in the climate change experiments. The error bars indicate the bootstrap estimates of the 95% confidence intervals. The values in the legends indicate the latitude shift between the control (global-mean SST of 288 K) and warm (global-mean SST of 300 K) cases. GR = gray radiation scheme; FB = four longwave-band scheme; WV = four longwave band with interactive water vapor scheme; RRTMG = Rapid Radiative Transfer Model for GCM; GCM = general circulation model; SST = sea surface temperature.

In contrast, the stratospheric cooling is overall stronger in the GCMs than in the RCE models, which is indicative of large-scale dynamical effects. The latitudinal contrast of the stratospheric temperature response (enhanced polar cooling and enhanced warming at around 35° latitude) in the GCMs does not occur in the RCE models.

4.3. Jet Stream and Storm Track

The zonal-mean zonal wind responses and the shift of the eddy-driven jet (maximum surface westerlies or maximum surface zonal wind stress) also vary among the radiation schemes (Figure 4, shading; Figure 7, left panel; Appendix C). GR shows a transition from split to merged jet regime as climate warms: its subtropical jet strengthens and gradually merges with the weakened eddy-driven jet that shifts equatorward (Figure 7, left panel, gray line). A similar equatorward shift of the surface westerlies was found to be associated with a transition from a double to a single jet regime in previous studies (Lachmy & Harnik, 2016; Lee & Kim, 2003; Son & Lee, 2005). In the GR experiment, the transition occurs near a global-mean SST of 293 K, and the relatively large uncertainty in the latitude of surface westerlies for this case (see the error bars for the gray line in the left panel of Figure 7) is due to the regime transition. The uncertainties for the other cases are small.

For other schemes, the subtropical and eddy-driven jets are merged in all climates, and consistently the jet variability and the uncertainty of the jet latitude estimate are very small (see the error bars for the colored lines in the left panel of Figure 7). In this case, the jet core intensifies and shifts upward as climate warms (Figure 4, three right panels), consistent with the increased tropical stability and the rise of the tropical tropopause (Shaw & Tan, 2018; Vallis et al., 2015). The jet shifts slightly poleward with FB (Figure 7, left panel, red line) and more significantly poleward with WV and RRTMG, indicated by the zonal wind deceleration in the subtropical middle troposphere (Figure 4, third and fourth panels) and poleward shift in the surface westerlies (Figure 7, left panel, amber and blue lines). The stronger poleward jet shifts in WV and RRTMG than FB are consistent with their larger increase in the middle and upper tropospheric ($0.2 \leq \sigma \leq 0.7$) temperature gradient across the midlatitudes (30° to 60°; compare the three top right panels of Figure 2), and they are also consistent with the CMIP5 models (e.g., Barnes & Polvani, 2013; Vallis et al., 2015).

The storm track shift is nonmonotonic (equatorward then poleward) for GR (Figure 7, right panel, gray line). In warm climates, its poleward storm track shift is opposite to its jet shift but consistent with the storm track shift of other radiation schemes. This poleward shift also occurs for alternative storm track metrics such as the eddy heat flux or the near-surface EKE (see Appendix C). Lachmy and Shaw (2018) provided a more detailed physical interpretation of the different responses of the eddy-driven jet and storm track in GRaM. For all other radiation schemes, the storm tracks shift robustly poleward as climate warms (Figure 7, right panel, colored lines). For WV and RRTMG, the magnitude of storm track shifts is comparable to the jet

shifts, except in the warmest climates (about 308 K) when the storm tracks shift further poleward (by about 8° latitude) than the jets. The uncertainties of the storm track position estimates are small for all cases.

5. Spectral Analysis and Jet Shift Mechanisms

Clearly the different radiation schemes lead to different jet stream climatologies (split versus merged jet) and radiative responses to warming, both of which affect their temperature and zonal wind responses. The most important difference between the different schemes is that the eddy-driven jet in GR shifts equatorward in response to warming whereas all the other schemes shift poleward. In this section, we examine the dynamical mechanisms that may contribute to the differences.

Various barotropic mechanisms have been proposed to explain the poleward shift of the eddy-driven jet in response to warming. The proposed mechanisms assume a strong warming response to increased greenhouse gases in the tropical upper troposphere, which is assumed to lead to increased eddy length scale (Kidston et al., 2011; Rivière, 2011) and enhanced upper tropospheric zonal-mean zonal wind in the subtropics and midlatitudes, via the thermal wind balance. On the one hand, an increase in the eddy length scale may lead to a poleward eddy-driven jet shift, either because it reduces the wave phase speed and allows eddies to propagate further poleward from the wave source, causing a poleward expansion of the net wave source region (Kidston et al., 2011), or because it favors anticyclonic wave breaking and increases equatorward wave propagation (Rivière, 2011). On the other hand, for a fixed eddy length scale, strengthened zonal wind on the poleward flank of the jet leads to an increased phase speed $c_{r,k}$ of the reflecting level (defined as the critical wave phase speed below which waves are reflected), and the resulting increase of wave reflection may also lead to a net increase in equatorward wave propagation and a poleward eddy-driven jet shift (Kidston & Vallis, 2012; Lorenz, 2014a, 2014b).

To test whether the simulated jet shift can be attributed to changes in the eddy length scale or wave reflection, we perform spectral analyses on the EMF and eddy streamfunction since it provides a cleaner measure of eddy amplitude. Mathematically, the EMF spectrum equals the eddy streamfunction variance spectrum multiplied by $-kl$, where k and l are the zonal and meridional wave numbers, respectively. This is because the velocities (u, v) are the y and the negative of x derivatives of the streamfunction, which correspond to multiplications by il and ik in the spectral space (Vallis, 2006, chapter 12, equations 12.5 to 12.10). If the poleward jet shift is associated with the eddy length scale mechanism, then the EMF zonal wave number spectrum should show a shift toward smaller wave numbers. If it is associated with the wave reflection mechanism, then the EMF wave phase speed spectrum should show increased poleward EMF around the phase speed $c_{r,k}$ of increased reflection (e.g., Lorenz, 2014b, Figure 12b). We would expect the opposite responses for the equatorward jet shift in GR, namely a shift of the EMF zonal wave number spectrum toward larger wave numbers and a decrease of the EMF wave phase speed spectrum around the phase speed $c_{r,k}$ of decreased reflection.

It is important to note that the eddy-mean flow interactions described in the following analyses do not explain the jet shift in terms of cause and effect, because they rely on the equilibrated zonal-mean flow response itself. Instead, these analyses enable us to diagnose the processes that take place, and rule out those explanations for the poleward jet shift that are inconsistent with the eddy-driven jet response for the different radiation schemes.

5.1. Climatological Spectra

In order to test the barotropic arguments for the poleward eddy-driven jet shift in response to warming, we need to first identify a single vertical level that is representative of the vertically integrated EMF spectra. In addition, in order to examine changes in the wave propagation properties, we need to focus on specific wave numbers that are most representative of the total EMF at the same vertical level.

We start with the climatological zonal wave number spectra of vertically integrated eddy streamfunction variance (Figure 8, top row, lines) and vertically integrated EMF (Figure 8, bottom row, lines). Both spectra show spectral peaks at wave numbers 3–5 for GR and wave numbers 5–7 for the other schemes. The wave number 5 variance that dominates the streamfunction variance of FB and RRTMG may be associated with resonant quasi-stationary waves (at phase speeds within ±5 m/s), which were seen in previous aquaplanet GCM studies (e.g., Hu et al., 2008; Watanabe, 2005) and interpreted as "baroclinic stationary waves" trapped in the jet stream (Zappa et al., 2011). These trapped waves do not have significant phase tilt and contribute

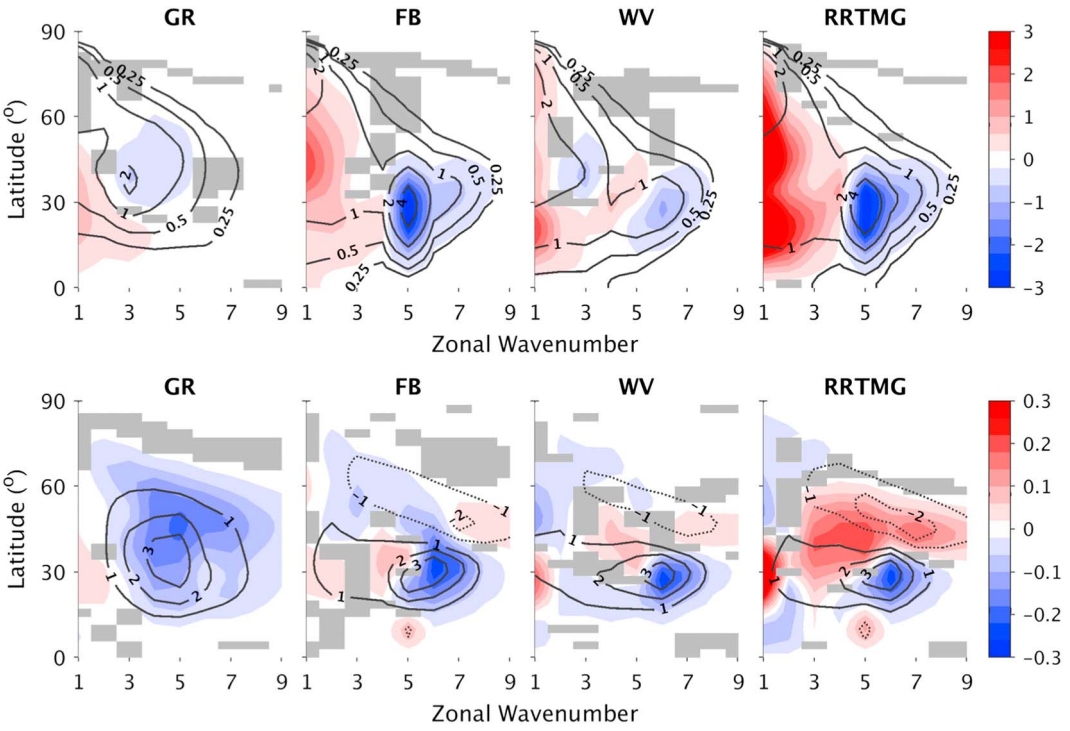

Figure 8. Mass-weighted vertically averaged zonal wave number spectra of (top row) eddy streamfunction variance for the control climate (lines, unit is 1013 m4/s2) and their response to warming normalized by global-mean SST increase (shading, unit is 1012 m4·s^{-2}·K^{-1}), and (bottom row) meridional eddy momentum flux for the control climate (lines, unit is m2/s2) and their response to warming normalized by global-mean SST increase (shading, unit is m2·s^{-2}·K^{-1}). (first column) GR = gray radiation scheme; (second column) FB = four longwave-band scheme; (third column) WV = four longwave band with interactive water vapor scheme; (fourth column) RRTMG = Rapid Radiative Transfer Model for GCM. Regions of statistically insignificant responses include gray shading. GCM = general circulation model; SST = sea surface temperature.

relatively little to the EMF, which is dominated by wave number 6. This wave resonance is absent in GR and is weak in WV. Additionally, the climatological zonal wave number spectra at a single level in the upper troposphere ($\sigma = 0.245$) are representative of the respective vertically integrated spectra for all cases, despite the tropopause being lower in GR than other schemes (compare lines between Figures 8 and 9).

Next we analyze the climatological wave phase speed spectra to investigate the wave propagation in the upper troposphere at $\sigma = 0.245$ (top panels of Figure 10, black lines). Climatologically, the GR scheme produces poleward EMF at all phase speeds and up to 60° latitude, indicating predominantly equatorward wave propagation. This is consistent with its broad jet and lack of polar surface easterlies, which are characteristic for a split jet regime dominated by eddy-driven jet (Lachmy & Harnik, 2016). In contrast, all other schemes produce equatorward EMF (and poleward wave propagation) at the poleward flank of the climatological jet, which is consistent with the sharper jet and polar surface easterlies; these features are similar to the merged jet regime described by Lachmy and Harnik (2016).

For GR, the zonal wave numbers $k = 4$ and 5 are the major contributors of the climatological EMF spectra (bottom left panel of Figure 9 and left column of the center and bottom panels of Figure 10, black lines). For all other schemes, the zonal wave number $k = 6$ accounts for the meridional dipole pattern of the EMF spectra around wave phase speed 7 m/s, whereas $k = 7$ accounts for the dipole at higher phase speeds around 10 m/s (three right columns of the center and bottom panels of Figure 10, black lines).

5.2. Response of Wave Number Spectra to Warming

The GR model shows a clear weakening of both eddy streamfunction variance and EMF spectra, as well as an equatorward shift of the EMF spectra (indicated by the stronger decrease at higher than lower latitudes), without a significant shift in the dominant wave number (Figures 8 and 9, left column). Also, some equatorward EMF emerges at the poleward flank of the jet in warm climates, consistent with the transition into a merged jet regime; the resulting EMF spectrum is more similar to the other schemes. In contrast, all

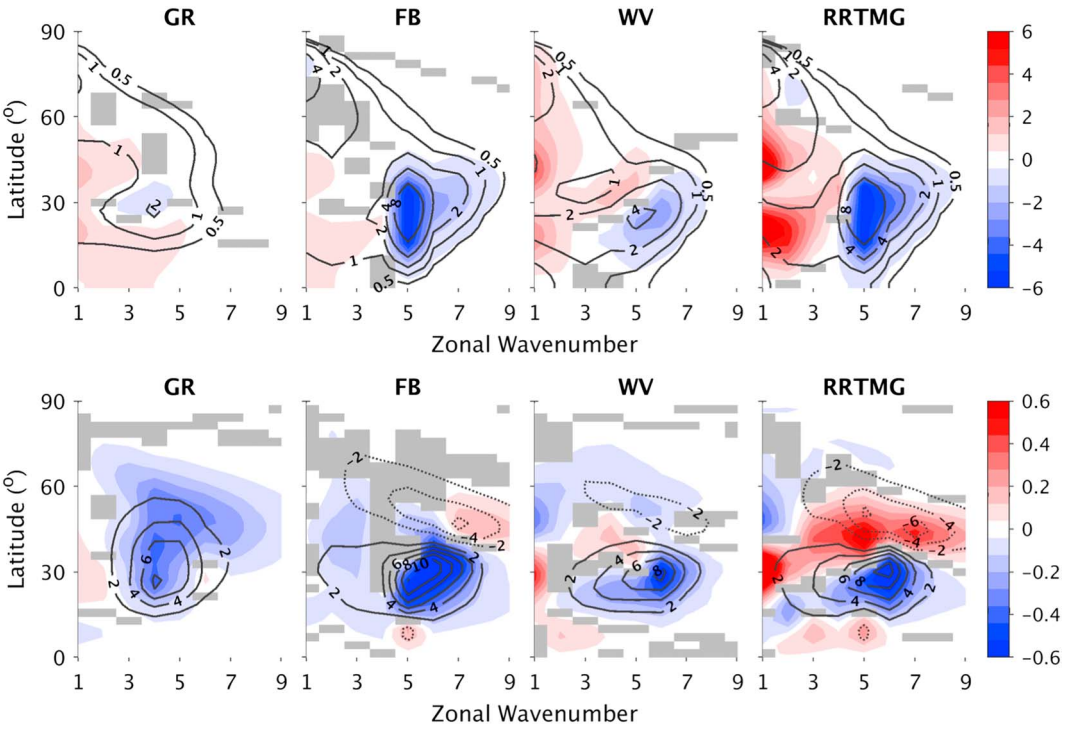

Figure 9. Same as Figure 8, but for single-level results at $\sigma = 0.245$. GR = gray radiation scheme; FB = four longwave-band scheme; WV = four longwave band with interactive water vapor scheme; RRTMG = Rapid Radiative Transfer Model for GCM; GCM = general circulation model.

other schemes show a shift to lower wave numbers, most remarkably for RRTMG and WV (Figures 8 and 9, three right columns). For RRTMG, the poleward EMF decreases on the equatorward flank (around 30°) and increases on the poleward flank (around 40°) of the jet for all wave numbers $k = 4$ to 9. The negative response peaks at the climatologically dominant wave number ($k = 6$) and the positive response peaks at lower wave numbers ($k = 4$ and 5). WV shows similar responses in its EMF spectrum (most noticeable in the bottom panels of Figure 8), although they are weaker (but still statistically significant) than RRTMG. This response is consistent with the "increased eddy length scale" mechanism of Rivière (2011) that larger eddies tend to break anticyclonically (rather than cyclonically) and contribute to poleward EMF, and that a shift to smaller wave number tends to increase poleward EMF and decrease equatorward EMF. As discussed by Rivière (2011), the shift toward small wave numbers is related to increased upper level baroclinicity, which destabilizes long waves and stabilizes short waves. This is consistent with the increased upper tropospheric vertical shear for the WV and RRTMG cases (Figure 4).

FB differs from WV and RRTMG in its EMF spectrum response. Despite a reduction in the dominant wave number, FB displays an overall decrease in the poleward EMF (Figures 8 and 9, second columns of bottom row), consistent with its weaker jet shift. The response of the streamfunction variance (Figures 8 and 9, second columns of top row) in FB also differs from WV and RRTMG: between 25° and 45° latitude, the wave number 4 streamfunction variance increases significantly with WV and RRTMG but not with FB. This difference may be related to the larger increase in poleward energy transport in WV and RRTMG due to water vapor feedback (section 4.1), which potentially leads to stronger lower-level eddy heat flux (and thus stronger wave source) compared to FB. However, its dynamical connection with the different responses in upper-level wave propagation and EMF requires further investigation.

5.3. Response of Wave Phase Speed Spectra to Warming

We now investigate the change in wave propagation by analyzing the response of the EMF wave phase speed spectra as climate warms. Based on the linearized barotropic assumption, poleward propagating Rossby waves are reflected equatorward as they reach the reflecting level (blue lines in the two lower rows of Figure 10), and then are absorbed at the critical level (where the eddy phase speed equals the zonal-mean zonal wind, magenta lines in Figure 10). The poleward propagating and equatorward reflected waves

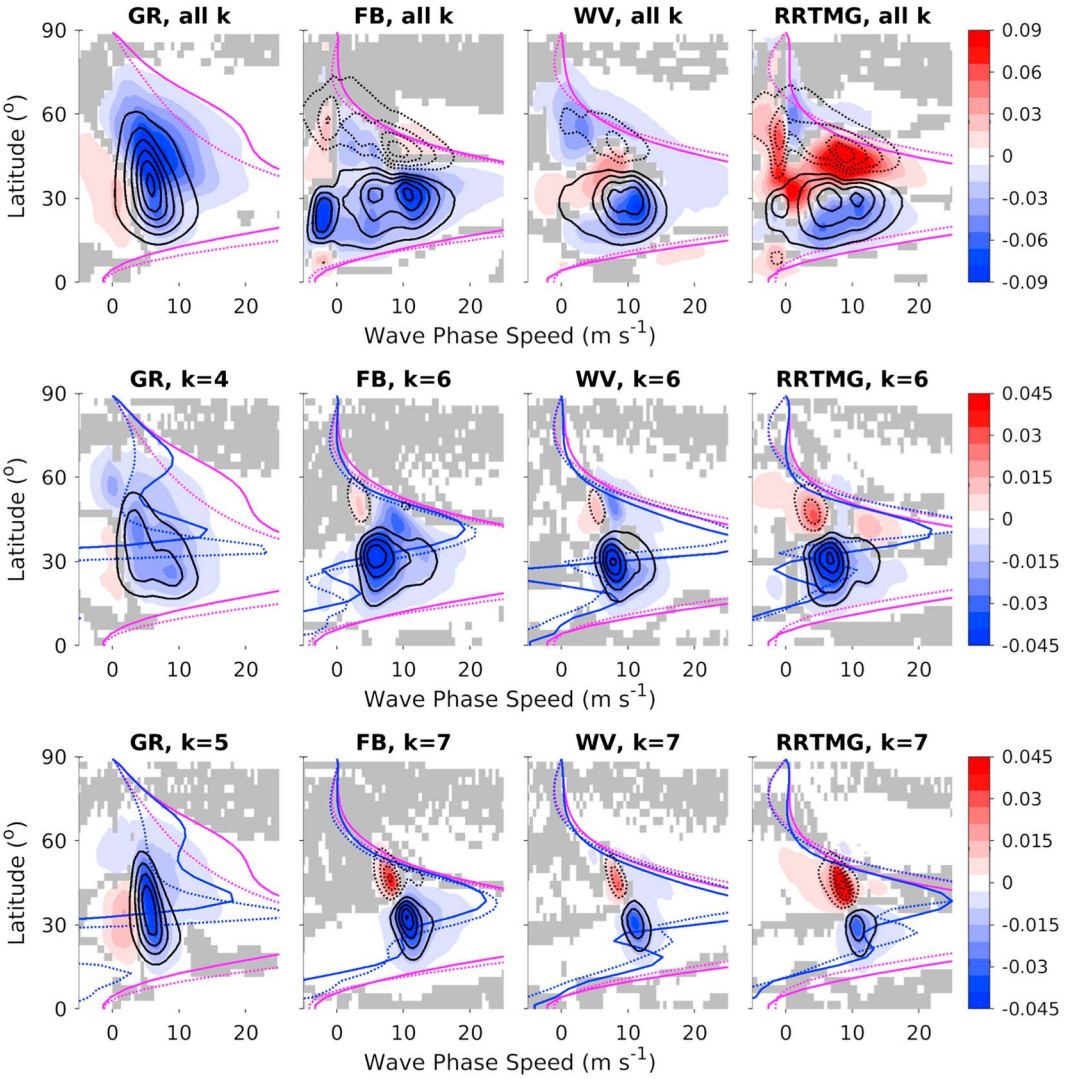

Figure 10. The wave phase speed spectra of meridional eddy momentum flux for the control climate (contour lines) and their response to warming normalized by global-mean SST increase (shading, unit is $m^2\ s^{-2}\cdot K^{-1}\cdot\Delta c^{-1}$) at σ = 0.245. (top row) Sum of all wave numbers. (center and bottom rows) Single zonal wave numbers k = 4 and 5 for GR and k = 6 and 7 for other schemes. (first column) GR = gray radiation scheme; (second column) FB = four longwave-band scheme; (third column) WV = four longwave band with interactive water vapor scheme; (fourth column) RRTMG = Rapid Radiative Transfer Model for GCM. The line intervals are 0.30 $m^2\cdot s^{-2}\cdot\Delta c^{-1}$ (top) and 0.15 $m^2\cdot s^{-2}\cdot\Delta c^{-1}$ (center and bottom), and the dotted lines represent negative values. The magenta lines represent the zonal-mean zonal wind, and the blue lines represent the phase speed of the reflecting level, for which the solid and dotted lines represent the control (global-mean SST of 288 K) and warm (global-mean SST of 300 K) climates, respectively. GCM = general circulation model; SST = sea surface temperature.

contribute to equatorward and poleward EMF respectively. If the reflecting level extends into higher phase speeds or if its latitudinal width expands, more Rossby waves are expected to be reflected equatorward, corresponding to increased poleward EMF and a poleward jet shift (Kidston & Vallis, 2012; Lorenz, 2014a, 2014b). Conversely, a decrease of the reflecting phase speed or a narrowing of the reflecting level corresponds to less wave reflection, reduced poleward EMF, and an equatorward jet shift. Furthermore, a poleward shift of the critical level or a reduction of dominant wave phase speed allows for Rossby waves to propagate further poleward before getting absorbed, corresponding to a poleward shift of the EMF pattern and eddy-driven jet (Kidston et al., 2011).

The GR model shows a general weakening of the EMF phase speed spectra. Additionally, the reflecting phase speed decreases poleward of 35° latitude as the jet narrows (first column of Figure 10, compare the blue lines), and correspondingly there is a reduction in the poleward EMF at wave phase speeds faster than the

warm climate reflecting level (around 5 m/s) at these latitudes. This is consistent with the wave reflection argument above and the equatorward jet shift. In contrast, the critical level mechanism does not apply: as the critical level on the poleward flank of the jet shifts equatorward (first column of Figure 10, compare the magenta lines), the EMF pattern does not simply shift equatorward, but it switches sign from positive to negative at latitudes poleward of 40° (not shown). Lachmy and Shaw (2018) also found that the change in the critical line does not explain the different eddy-driven jet and storm track responses in the GR model.

All the other radiation schemes show preferential reduction of poleward EMF on the equatorward flank of the jet when summing over all wave numbers (the three top right panels of Figure 10), consistent with the wave number spectra results discussed above. The wave reflection mechanism of Lorenz (2014a, 2014b) does not contribute significantly to the change of EMF and the jet shift, since the change in the reflecting level is small at the phase speed range of significant EMF for the dominant wave numbers $k = 5$ (not shown), 6 and 7 (three right columns of Figure 10). Instead, the $k = 6$ and 7 spectrum responses are characterized by the weakening of the climatological patterns, associated with the shift toward smaller dominant wave numbers (discussed in section 5.2).

6. Conclusions and Discussions

A new clear-sky LW radiation hierarchy is configured in a slab ocean aquaplanet GCM and used to quantify how radiative assumptions affect the jet stream and storm track responses to warming. The radiation hierarchy includes a GR scheme, a four LW band scheme without or with interactive water vapor (FB and WV, respectively), and a correlated-*k* (RRTMG) scheme. The jet stream and storm track and their responses to warming vary among the radiation schemes, even with similar SST distribution and response. The key results are summarized as follows:

1. Climatologically, the GR scheme produces a relatively warm and low tropopause, and a large stratospheric temperature gradient between the midlatitudes and the poles. This thermal structure corresponds to a split jet pattern consisting of a shallow subtropical jet, a broad and poleward eddy-driven jet, and a strong stratospheric polar vortex. In contrast, all other radiation schemes with multiple LW bands produce a cooler stratosphere and a higher tropopause corresponding to a merged and more equatorward jet. The inclusion of interactive water vapor also leads to larger EIA in the tropics and stronger poleward energy transport.
2. As climate warms, the GR scheme undergoes a jet regime transition: its subtropical and eddy-driven jets merge as the tropopause rises, surface westerlies shift equatorward, whereas the storm track shifts equatorward then poleward. All other schemes maintain a merged jet, and their storm tracks and surface westerlies shift robustly poleward as climate warms. The four LW band scheme without water vapor produces a weaker tropical-subtropical amplification of the EIA response, corresponding to a smaller increase in poleward energy transport and a weaker poleward shift in the surface westerlies compared to schemes with interactive water vapor.
3. From a dynamical perspective, the equatorward jet shift with the GR scheme is related to the reduction of wave reflection on the poleward flank of the jet, whereas the poleward jet shift with the other schemes is related to an increase in eddy length scale that favors equatorward over poleward wave propagation.

The results highlight the impact of radiation on the thermodynamic and circulation responses to warming that are independent of changes in SST and SST gradient. The response to climate change for the gray radiation scheme (equatorward jet shift) can clearly be traced to the gray radiation assumption and lack of interactive water vapor. The radiation hierarchy suggests that gray radiation is not sophisticated enough to capture the circulation response to warming. Consequently, we recommend that the simplest radiative scheme used to study the extratropical circulation should have multiple (preferably at least four) LW bands with simplified dependence (e.g., linear) on water vapor.

Previous studies have shown that the intermodel variability of extratropical jet and storm track responses as climate warms are partly attributed to their different control climates (Kidston & Gerber, 2010; Simpson & Polvani, 2016). The control climates also differ significantly across our radiation hierarchy: even though the LW opacity parameters are carefully calibrated so as to reproduce the climatological SST of the RRTMG model, the climatological temperature and zonal wind profiles are still sensitive to the choice of radiation scheme. By comparing GR with the other schemes, we show that the jet and storm track responses, as well as the underlying wave-mean flow interaction mechanisms, are sensitive to the climatological jet regime.

The radiation hierarchy introduced here focuses on clear-sky LW radiation. Many additional processes should be added including the ozone layer and clouds. However, the GFDL AM2.1 model that includes these components also produces a merged jet that shifts poleward at a similar rate normalized by the global-mean SST increase (Ceppi & Hartmann, 2016; Shaw & Tan, 2018) as our simplified RRTMG model. This hints that our simplified RRTMG model may have captured the essential processes that shape the extratropical circulation response to warming.

This study and Lachmy and Shaw (2018) both demonstrate that a radiation hierarchy combined with a dynamical theory can help improve our understanding of the shift of the storm track and eddy-driven jet in response to warming. More generally, this combined radiative-dynamical perspective will likely be useful for understanding other radiation-induced circulation responses, such as the response of extratropical circulation variability (e.g., the annular mode patterns and time scales) and the tropical circulation (e.g., the Hadley cell).

Appendix A: Stratospheric Radiative Effects With Multiple LW Bands

The two major radiative effects of adding multiple LW bands to the gray scheme are to cool down the stratosphere in the control climate and to induce a global-mean stratospheric cooling as SST warms.

A1. Cooler Stratosphere

The cooler stratosphere with multiple LW bands can be understood from the radiative balance near TOA. If there is neither dynamical nor SW heating, a slab of air near TOA should be in LW radiative balance. For gray radiation, its temperature T_{TOA} satisfies

$$2\sigma_b \epsilon T_{\mathrm{TOA}}^4 = \epsilon \mathrm{OLR}, \tag{A1}$$

where $\epsilon \ll 1$ is the LW emissivity of the slab, σ_b is the Stefan-Boltzmann constant, and OLR is the outgoing LW radiation at TOA. This can be rearranged as

$$T_{\mathrm{TOA}} = 2^{-1/4}(\mathrm{OLR}/\sigma_b)^{1/4} \equiv 2^{-1/4} T_e, \tag{A2}$$

where T_e is the emission temperature (Schneider, 2007). Plugging in OLR = 238 W/m^2 from the GR cases, this formula gives $T_{\mathrm{TOA}} = 214$ K, which is very close to the simulated global-mean TOA temperature in the GR cases (left panel of Figure A1, solid lines).

If there are multiple LW bands, and each band spreads widely across the entire LW spectrum (so that the Stefan-Boltzmann law roughly holds for individual bands), the slab radiative balance is:

$$2\sigma_b \left(\sum_i w_i \epsilon_i \right) T_{\mathrm{TOA}}^4 = \sum_i \left(w_i \epsilon_i \mathrm{OLR}_i \right), \tag{A3}$$

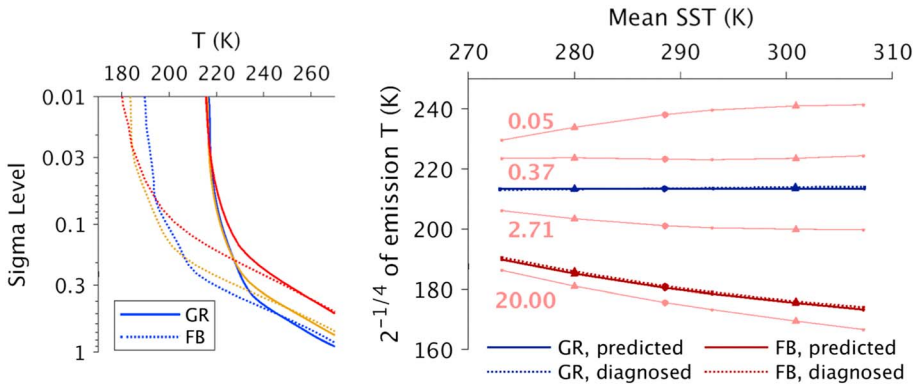

Figure A1. (left) The vertical profiles of global-mean temperature. Blue, amber, and red lines represent the cool, control, and warm climates (global-mean SST of 280, 288, and 300 K, respectively). (right) The global-mean top-of-atmosphere temperature predicted from outgoing longwave radiation using equations (A2) and (A4), compared with the diagnosed GCM values. The thinner lines represent the global-mean $2^{-1/4} T_{e,i}$ of all four longwave bands in the FB model, and the numbers represent their relative longwave emissivities.

where subscript i represents the i-th band, w_i is its spectral width ($\sum_i w_i = 1$), ϵ_i and OLR_i are its LW emissivity and its outgoing LW radiation normalized by w_i. This can be again rearranged as:

$$T_{\mathrm{TOA}} = 2^{-1/4}(\mathrm{OLR}_m/\sigma_b)^{1/4} \equiv 2^{-1/4}T_{e,m}, \tag{A4}$$

where OLR_m is the weighted average of OLR_i by band width $w_i\epsilon_i$, and $T_{e,m}$ is the corresponding bulk emission temperature. Given that in general a band with large ϵ_i at TOA is also optically thick throughout the atmospheric column, it should emit at a high altitude with a small OLR_i, and thus the weighted average OLR_m and emission temperature $T_{e,m}$ should be smaller than the total OLR($= \sum_i w_i \mathrm{OLR}_i$) and T_e. Therefore, the inclusion of multiple LW bands generally leads to $T_{\mathrm{TOA}} < 2^{-1/4}T_e$.

We may even deduce a quantitative estimate of T_{TOA} for the FB scheme. The emission level of its thickest band is about $\log(20)/4 = 0.75$ scale heights (see section 2.2.2) or about 6 km higher than the bulk emission level of 255 K. Assuming a 6.5 K lapse rate, this corresponds to $T_{e,1} \approx 216$ K and $T_{\mathrm{TOA}} \approx 2^{-1/4}T_{e,1} = 182$ K, which is close to the simulated global-mean TOA temperature in the FB cases (left panel of Figure A1, dotted lines).

A2. Further Stratospheric Cooling as SST Warms

With multiple LW bands, the stratosphere can cool as SST (or lower tropospheric temperature) warms, even in the absence of ozone-induced stratospheric SW heating and without increased stratospheric LW emissivity. This is discussed by Goessling and Bathiany (2016) as the "blocking effect" and can be understood as follows (Figure A1, right panel): for steady state and assuming unchanged TOA albedo, the total OLR should balance the net absorbed SW radiation and remain unchanged, but the OLR of thinner bands (which act like spectral windows) increases as the surface and the lower troposphere become warmer (the top light red line). To compensate, the OLR of the thicker bands must decrease (the lower light red lines), which leads to decreased $T_{e,m}$ and T_{TOA} (the thick red lines). This cooling mechanism, however, cannot occur with a gray scheme, whose T_{TOA} depends solely on the total OLR that remains unchanged (the thick blue lines).

In fact, equations (A2) and (A4) can predict almost exactly the TOA temperature in the GCM (compare thick solid and dashed lines). This is because the sponge layer (see section 2.1) strongly damps the dynamics in the GCM, and thus a pure radiative equilibrium is maintained near the TOA.

A3. Indirect Cooling and Greenhouse Warming

Even as LW emissivity increases, the stratosphere with a gray scheme can only cool if there exists some external heating, such as SW absorption ("indirect solar effect" in Goessling and Bathiany (2016)) or dynamical heating, which is discussed in more details by Vallis et al. (2015). This indirect cooling effect also occurs with multiple-band LW schemes. With an ozone layer, this effect contributes to significant stratospheric cooling. Goessling and Bathiany (2016) quantified its contribution to the total CO_2-induced cooling of Earth's middle atmosphere in comparison with the "blocking effect" discussed above, and they reported that the "indirect solar effect" contributed up to 70% of the total cooling around the stratopause but only about 40% above and below the stratopause. This SW-induced indirect cooling is not significant in our study, because the stratospheric SW heating is very weak in the absence of the ozone layer; it will be further investigated in future studies with an ozone layer.

The spatially dependent indirect cooling (heating) effect may still occur where there is dynamical heating (cooling). This may explain some of the meridional contrast of stratospheric temperature responses in our GCM study: the polar stratosphere subject to dynamical heating tends to cool as LW emissivity increases, and vice versa for the tropical stratosphere. However, this indirect response is complicated by the direct dynamical effects due to circulation changes.

Additionally, a weak greenhouse warming response may occur as the LW opacity aloft increases. As is stated by Vallis et al. (2015) (their equation (13) and the subsequent discussions), whether the indirect cooling or the greenhouse warming dominates depends on the LW opacity: the indirect cooling dominates at the TOA and the upper stratosphere where the LW opacity is very small, whereas the greenhouse warming becomes increasingly important at lower altitudes where the LW opacity is larger.

Appendix B: Slab Ocean Radiative-Convective Equilibrium Models

In the aquaplanet GCM, the poleward energy transport by atmospheric circulation leads to net cooling in the tropics and net heating in the extratropics. In the RCE model there is no atmospheric energy transport, and

thus its tropics is warmer than the GCM if no external cooling is imposed (and vice versa for the extratropics). Especially for radiation schemes with water vapor feedback (WV and RRTMG), the deep tropics may enter a runaway greenhouse state and fail to equilibrate (Pierrehumbert, 1995).

An intuitive fix for the excessive tropical warming is to impose the tropical cooling by atmospheric circulation (diagnosed from EIA in the aquaplanet GCMs) as an ocean cooling term in the RCE models, so that the coupled energy budget of the atmosphere for the RCE models and GCMs are comparable. This approach resolves most of the SST biases in RCE models if their radiation schemes do not include water vapor feedback (GR and FB). However, for radiation schemes with water vapor feedback (WV and RRTMG), the RCE models produce excessive warming in the subtropics. This is because the RCE model lacks large-scale subsidence drying, and its ubiquitous convection causes a much moister subtropics than the GCM, corresponding to a stronger local greenhouse effect. To prevent this subtropical warm bias, it is necessary to prescribe the specific humidity as an input for the WV and RRTMG schemes, so as to ensure that the LW opacity (and thus the SST) is similar at all latitudes between the RCE model and the GCM.

Appendix C: Alternative Metrics of Eddy-Driven Jet and Storm Track Position

To verify that the eddy-driven jet and storm track responses are qualitatively insensitive to the choice of metrics, we repeat our analyses with three alternative metrics: for the eddy-driven jet we use the surface zonal wind stress, and for the storm track we use (1) the vertically integrated poleward eddy heat flux and (2) the near-surface EKE, defined as the vertically integrated EKE below $\sigma = 0.85$. The storm track metrics are mass-weighted and area-weighted as the DSE flux analysis.

The eddy-driven jet latitudes based on zonal wind stress are almost identical to those based on surface westerlies (compare the top panel of Figure C1 with the left panel of Figure 4), since the zonal wind stress generally increases with surface zonal wind (there is no topography or surface roughness variation in our aquaplanet model). Both storm track metrics show equatorward-then-poleward shifts of the GR storm track, and monotonically poleward shifts of the FB, WV, and RRTMG storm tracks, which are qualitatively con-

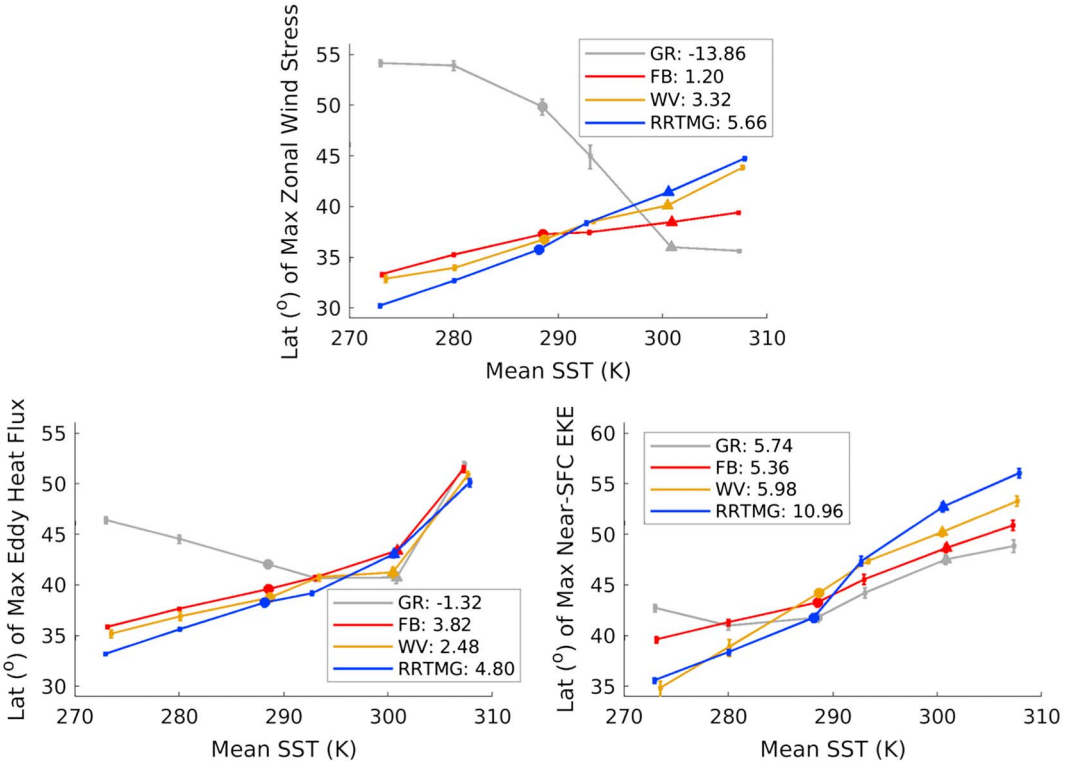

Figure C1. Same as Figure 4 but for (top) surface zonal wind stress, (bottom left) vertically integrated poleward eddy heat flux, and (bottom right) near-surface eddy kinetic energy. GR = gray radiation scheme; FB = four longwave-band scheme; WV = four longwave band with interactive water vapor; RRTMG = Rapid Radiative Transfer Model for GCM; GCM = general circulation model; SST = sea surface temperature.

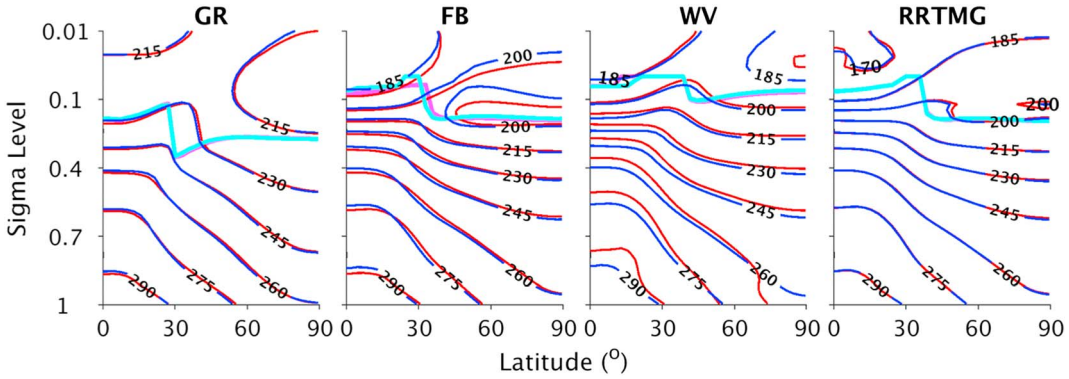

Figure D1. Climatological zonal-mean temperature from the slab ocean (red lines) and fixed SST (blue lines) experiments (unit is K). From left to right, (first panel) GR = gray radiation scheme; (second panel) FB = four longwave-band scheme; (third panel) WV = four longwave band with interactive water vapor scheme; (fourth panel) RRTMG = Rapid Radiative Transfer Model for GCM. The thick cyan and magenta lines indicate the climatological tropopause for the slab ocean and fixed SST cases, respectively. GCM = general circulation model; SST = sea surface temperature.

sistent with results based on the DSE flux metric (compare the bottom panels of Figure C1 with the right panel of Figure 4). The eddy heat flux metric is particularly similar to the DSE flux metric, because the eddy heat flux dominates the eddy DSE flux and the eddy potential energy flux is an order of magnitude weaker (Lachmy & Shaw, 2018). The storm track positions based on the near-surface EKE metric are close to those based on the eddy DSE flux metric in the control climates, but they shift more strongly poleward between the control and the representative warm climates. The uncertainties of the estimates are small despite a comparably larger variability of the EKE-based storm track position.

Appendix D: Comparison With Fixed SST Experiments

To verify that the SST differences between the radiation schemes do not affect the climatological temperature structure and jet regime, we perform additional experiments with the control radiation parameters of each scheme and with the SST fixed at the time mean zonal-mean values of the RRTMG climatology. The results are shown in Figures D1 and D2.

There are minor qualitative differences between the slab ocean and fixed SST results. For example, the FB jet in the slab ocean run is slightly more poleward than in the fixed SST run, consistent with its warmer subtropical SST than RRTMG (Figure 5). The WV slab ocean run shows a cooler polar boundary layer but warmer tropics and free troposphere; its jet is correspondingly stronger than that in the

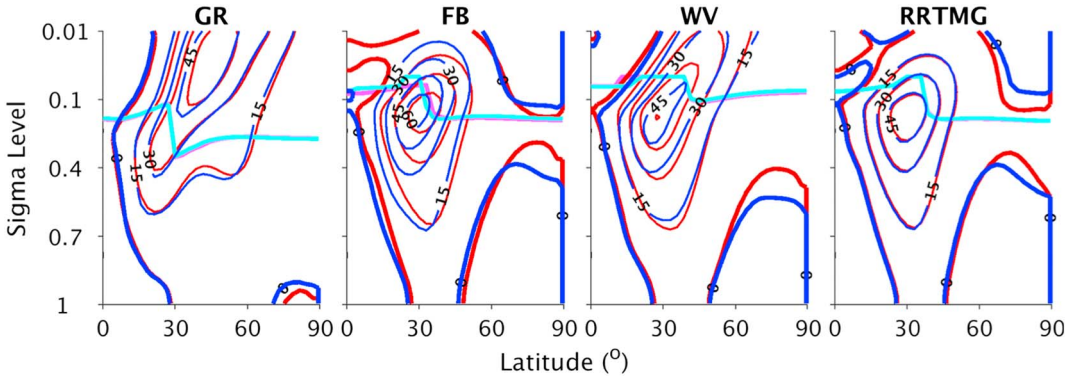

Figure D2. Same as Figure D1 but for zonal-mean zonal wind (unit is m/s, thick red and blue lines indicate zero winds). From left to right, (first panel) GR = gray radiation scheme; (second panel) FB = four longwave-band scheme; (third panel) WV = four longwave band with interactive water vapor scheme; (fourth panel) RRTMG = Rapid Radiative Transfer Model for GCM. GCM = general circulation model.

fixed SST run. Apart from these differences, the vertical structures of temperature and zonal wind and the tropopause heights are remarkably similar between the fixed SST and slab ocean experiments for all four radiation schemes.

Acknowledgments
Z. T., O. L., and T. A. S. acknowledge support from the National Science Foundation (AGS-1538944, AGS-1742944) and the David and Lucile Packard Foundation. Z. T., O. L., and T. A. S. thank Pragallva Barpanda for providing the analysis codes, and Elizabeth Maroon for providing the slab ocean version of the GFDL AM2.1 model. The simulations in this paper were completed with resources provided by the University of Chicago Research Computing Center. The radiation package and sample namelists are available for download on Zenodo (https://doi.org/10.5281/zenodo.2591764).

References

Barnes, E. A., & Polvani, L. (2013). Response of the midlatitude jets, and of their variability, to increased greenhouse gases in the CMIP5 models. *Journal of Climate*, *26*(18), 7117–7135. https://doi.org/10.1175/JCLI-D-12-00536.1

Barpanda, P., & Shaw, T. (2017). Using the moist static energy budget to understand storm-track shifts across a range of time scales. *Journal of the Atmospheric Sciences*, *74*(8), 2427–2446. https://doi.org/10.1175/JAS-D-17-0022.1

Beucler, T., & Cronin, T. W. (2016). Moisture-radiative cooling instability. *Journal of Advances in Modeling Earth Systems*, *8*, 1620–1640. https://doi.org/10.1002/2016MS000763

Blackburn, M., & Hoskins, B. J. (2013). Context and aims of the aqua-planet experiment. *Journal of the Meteorological Society of Japan Series II*, *91A*, 1–15. https://doi.org/10.2151/jmsj.2013-A01

Bony, S., Stevens, B., Frierson, D. M. W., Jakob, C., Kageyama, M., Pincus, R., et al. (2015). Clouds, circulation and climate sensitivity. *Nature Geoscience*, *8*, 261–268. https://doi.org/10.1038/ngeo2398

Byrne, M. P., & O'Gorman, P. A. (2012). Land–ocean warming contrast over a wide range of climates: Convective quasi-equilibrium theory and idealized simulations. *Journal of Climate*, *26*(12), 4000–4016. https://doi.org/10.1175/JCLI-D-12-00262.1

Ceppi, P., & Hartmann, D. L. (2016). Clouds and the atmospheric circulation response to warming. *Journal of Climate*, *29*(2), 783–799. https://doi.org/10.1175/JCLI-D-15-0394.1

Chang, E. K. M., Guo, Y., & Xia, X. (2012). CMIP5 multimodel ensemble projection of storm track change under global warming. *Journal of Geophysical Research*, *117*, D23118. https://doi.org/10.1029/2012JD018578

Delworth, T. L., Broccoli, A. J., Rosati, A., Stouffer, R. J., Balaji, V., Beesley, J. A., et al. (2006). GFDL's CM2 global coupled climate models. Part I: Formulation and simulation characteristics. *Journal of Climate*, *19*(5), 643–674. https://doi.org/10.1175/JCLI3629.1

Dwyer, J. G., & O'Gorman, P. A. (2017). Moist formulations of the Eliassen–Palm flux and their connection to the surface westerlies. *Journal of the Atmospheric Sciences*, *74*(2), 513–530. https://doi.org/10.1175/JAS-D-16-0111.1

Frierson, D. M. W. (2007). The dynamics of idealized convection schemes and their effect on the zonally averaged tropical circulation. *Journal of the Atmospheric Sciences*, *64*(6), 1959–1976. https://doi.org/10.1175/JAS3935.1

Frierson, D. M. W., Held, I. M., & Zurita-Gotor, P. (2006). A gray-radiation aquaplanet moist GCM. Part I: Static stability and eddy scale. *Journal of the Atmospheric Sciences*, *63*(10), 2548–2566. https://doi.org/10.1175/JAS3753.1

GFDL-GAMDT (2004). The new GFDL global atmosphere and land model AM2–LM2: Evaluation with prescribed SST simulations. *Journal of Climate*, *17*(24), 4641–4673. https://doi.org/10.1175/JCLI-3223.1

Goessling, H. F., & Bathiany, S. (2016). Why CO_2 cools the middle atmosphere—A consolidating model perspective. *Earth System Dynamics*, *7*(3), 697–715. https://doi.org/10.5194/esd-7-697-2016

Haqq-Misra, J., Lee, S., & Frierson, D. M. W. (2011). Tropopause structure and the role of eddies. *Journal of the Atmospheric Sciences*, *68*(12), 2930–2944. https://doi.org/10.1175/JAS-D-11-087.1

Hu, Y., Yang, D., & Yang, J. (2008). Blocking systems over an aqua planet. *Geophysical Research Letters*, *35*, L19818. https://doi.org/10.1029/2008GL035351

Iacono, M. J., Delamere, J. S., Mlawer, E. J., Shephard, M. W., Clough, S. A., & Collins, W. D. (2008). Radiative forcing by long-lived greenhouse gases: Calculations with the AER radiative transfer models. *Journal of Geophysical Research*, *113*, D13103. https://doi.org/10.1029/2008JD009944

Jucker, M., & Gerber, E. P. (2017). Untangling the annual cycle of the tropical tropopause layer with an idealized moist model. *Journal of Climate*, *30*(18), 7339–7358. https://doi.org/10.1175/JCLI-D-17-0127.1

Kang, S. M., Held, I. M., Frierson, D. M. W., & Zhao, M. (2008). The response of the ITCZ to extratropical thermal forcing: Idealized slab-ocean experiments with a GCM. *Journal of Climate*, *21*(14), 3521–3532. https://doi.org/10.1175/2007JCLI2146.1

Kidston, J., & Gerber, E. P. (2010). Intermodel variability of the poleward shift of the austral jet stream in the CMIP3 integrations linked to biases in 20th century climatology. *Geophysical Research Letters*, *37*, L09708. https://doi.org/10.1029/2010GL042873

Kidston, J., & Vallis, G. K. (2012). The relationship between the speed and the latitude of an eddy-driven jet in a stirred barotropic model. *Journal of the Atmospheric Sciences*, *69*(11), 3251–3263. https://doi.org/10.1175/JAS-D-11-0300.1

Kidston, J., Vallis, G. K., Dean, S. M., & Renwick, J. A. (2011). Can the increase in the eddy length scale under global warming cause the poleward shift of the jet streams? *Journal of Climate*, *24*(14), 3764–3780. https://doi.org/10.1175/2010JCLI3738.1

Lachmy, O., & Harnik, N. (2016). Wave and jet maintenance in different flow regimes. *Journal of the Atmospheric Sciences*, *73*(6), 2465–2484. https://doi.org/10.1175/JAS-D-15-0321.1

Lachmy, O., & Shaw, T. (2018). Connecting the energy and momentum flux response to climate change using the Eliassen and Palm relation. *Journal of Climate*, *31*, 7401–7416. https://doi.org/10.1175/JCLI-D-17-0792.1

Lee, S., & Kim, H. (2003). The dynamical relationship between subtropical and eddy-driven jets. *Journal of the Atmospheric Sciences*, *60*(12), 1490–1503. https://doi.org/10.1175/1520-0469(2003)060<1490:TDRBSA>2.0.CO;2

Li, L. F. J., Waliser, D. E., Stephens, G., Lee, S., L'Ecuyer, T., Kato, S., et al. (2013). Characterizing and understanding radiation budget biases in CMIP3/CMIP5 GCMs, contemporary GCM, and reanalysis. *Journal of Geophysical Research: Atmospheres*, *118*, 8166–8184. https://doi.org/10.1002/jgrd.50378

Lin, S.-J. (2004). A "vertically Lagrangian" finite-volume dynamical core for global models. *Monthly Weather Review*, *132*(10), 2293–2307. https://doi.org/10.1175/1520-0493(2004)132<2293:AVLFDC>2.0.CO;2

Lorenz, D. J. (2014a). Understanding midlatitude jet variability and change using Rossby wave chromatography: Poleward-shifted jets in response to external forcing. *Journal of the Atmospheric Sciences*, *71*(7), 2370–2389. https://doi.org/10.1175/JAS-D-13-0200.1

Lorenz, D. J. (2014b). Understanding midlatitude jet variability and change using Rossby wave chromatography: Wave–mean flow interaction. *Journal of the Atmospheric Sciences*, *71*(10), 3684–3705. https://doi.org/10.1175/JAS-D-13-0201.1

Lu, J., Chen, G., & Frierson, D. M. W. (2010). The position of the midlatitude storm track and eddy-driven westerlies in aquaplanet AGCMs. *Journal of the Atmospheric Sciences*, *67*(12), 3984–4000. https://doi.org/10.1175/2010JAS3477.1

Manabe, S., & Strickler, R. F. (1964). Thermal equilibrium of the atmosphere with a convective adjustment. *Journal of the Atmospheric Sciences*, *21*(4), 361–385. https://doi.org/10.1175/1520-0469(1964)021<0361:TEOTAW>2.0.CO;2

Manabe, S., & Wetherald, R. T. (1975). The effects of doubling the CO_2 concentration on the climate of a general circulation model. *Journal of the Atmospheric Sciences*, *32*(1), 3–15. https://doi.org/10.1175/1520-0469(1975)032<0003:TEODTC>2.0.CO;2

Medeiros, B., Stevens, B., & Bony, S. (2015). Using aquaplanets to understand the robust responses of comprehensive climate models to forcing. *Climate Dynamics*, *44*(7), 1957–1977. https://doi.org/10.1007/s00382-014-2138-0

Merlis, T. M., & Schneider, T. (2011). Changes in zonal surface temperature gradients and walker circulations in a wide range of climates. *Journal of Climate*, *24*(17), 4757–4768. https://doi.org/10.1175/2011JCLI4042.1

O'Gorman, P. A., & Schneider, T. (2007). Recovery of atmospheric flow statistics in a general circulation model without nonlinear eddy-eddy interactions. *Geophysical Research Letters*, *34*, L22801. https://doi.org/10.1029/2007GL031779

O'Gorman, P. A., & Schneider, T. (2008a). Energy of midlatitude transient eddies in idealized simulations of changed climates. *Journal of Climate*, *21*(22), 5797–5806. https://doi.org/10.1175/2008JCLI2099.1

O'Gorman, P. A., & Schneider, T. (2008b). The hydrological cycle over a wide range of climates simulated with an idealized GCM. *Journal of Climate*, *21*(15), 3815–3832. https://doi.org/10.1175/2007JCLI2065.1

O'Rourke, A. K., & Vallis, G. K. (2013). Jet interaction and the influence of a minimum phase speed bound on the propagation of eddies. *Journal of the Atmospheric Sciences*, *70*(8), 2614–2628. https://doi.org/10.1175/JAS-D-12-0303.1

Pierrehumbert, R. T. (1995). Thermostats, radiator fins, and the local runaway greenhouse. *Journal of the Atmospheric Sciences*, *52*(10), 1784–1806. https://doi.org/10.1175/1520-0469(1995)052<1784:TRFATL>2.0.CO;2

Randel, W. J., & Held, I. M. (1991). Phase speed spectra of transient eddy fluxes and critical layer absorption. *Journal of the Atmospheric Sciences*, *48*(5), 688–697. https://doi.org/10.1175/1520-0469(1991)048<0688:PSSOTE>2.0.CO;2

Reichler, T., Dameris, M., & Sausen, R. (2003). Determining the tropopause height from gridded data. *Geophysical Research Letters*, *30*(20), 2042. https://doi.org/10.1029/2003GL018240

Rivière, G. (2011). A dynamical interpretation of the poleward shift of the jet streams in global warming scenarios. *Journal of the Atmospheric Sciences*, *68*(6), 1253–1272. https://doi.org/10.1175/2011JAS3641.1

Schneider, T. (2007). The thermal stratification of the extratropical troposphere. In T. Schneider & A. Sobel (Eds.), *The global circulation of the atmosphere* (pp. 47–77). Princeton: Princeton University Press.

Schneider, T., O'Gorman, P. A., & Levine, X. J. (2010). Water vapor and the dynamics of climate changes. *Reviews of Geophysics*, *48*, RG3001. https://doi.org/10.1029/2009RG000302

Shaw, T. A., Baldwin, M., Barnes, E. A., Caballero, R., Garfinkel, C. I., Hwang, Y. T., et al. (2016). Storm track processes and the opposing influences of climate change. *Nature Geoscience*, *9*, 656–664. https://doi.org/10.1038/ngeo2783

Shaw, T. A., Barpanda, P., & Donohoe, A. (2018). A moist static energy framework for zonal-mean storm-track intensity. *Journal of the Atmospheric Sciences*, *75*(6), 1979–1994. https://doi.org/10.1175/JAS-D-17-0183.1

Shaw, T. A., & Tan, Z. (2018). Testing some latitudinally-dependent explanations of the circulation response to increased CO_2 using aquaplanet models. *Geophysical Research Letters*, *45*, 9861–9869. https://doi.org/10.1029/2018GL078974

Shaw, T. A., & Voigt, A. (2016). What can moist thermodynamics tell us about circulation shifts in response to uniform warming? *Geophysical Research Letters*, *43*, 4566–4575. https://doi.org/10.1002/2016GL068712

Simpson, I. R., & Polvani, L. M. (2016). Revisiting the relationship between jet position, forced response, and annular mode variability in the southern midlatitudes. *Geophysical Research Letters*, *43*, 2896–2903. https://doi.org/10.1002/2016GL067989

Singh, M. S., & O'Gorman, P. A. (2012). Upward shift of the atmospheric general circulation under global warming: Theory and simulations. *Journal of Climate*, *25*(23), 8259–8276. https://doi.org/10.1175/JCLI-D-11-00699.1

Son, S. W., & Lee, S. (2005). The response of westerly jets to thermal driving in a primitive equation model. *Journal of the Atmospheric Sciences*, *62*(10), 3741–3757. https://doi.org/10.1175/JAS3571.1

Stephens, G. L., & L'Ecuyer, T. (2015). The earth's energy balance. *Atmospheric Research*, *166*, 195–203. https://doi.org/10.1016/j.atmosres.2015.06.024

Vallis, G. K. (2006). *Atmospheric and oceanic fluid dynamics*. Cambridge, UK: Cambridge University Press.

Vallis, G. K., Colyer, G., Geen, R., Gerber, E., Jucker, M., Maher, P., et al. (2018). Isca, v1.0: A framework for the global modelling of the atmospheres of earth and other planets at varying levels of complexity. *Geoscientific Model Development*, *11*(3), 843–859. https://doi.org/10.5194/gmd-11-843-2018

Vallis, G. K., Zurita-Gotor, P., Cairns, C., & Kidston, J. (2015). Response of the large-scale structure of the atmosphere to global warming. *Quarterly Journal of the Royal Meteorological Society*, *141*(690), 1479–1501. https://doi.org/10.1002/qj.2456

Voigt, A., & Shaw, T. A. (2015). Circulation response to warming shaped by radiative changes of clouds and water vapour. *Nature Geoscience*, *8*, 102–106. https://doi.org/10.1038/ngeo2345

Voigt, A., & Shaw, T. A. (2016). Impact of regional atmospheric cloud radiative changes on shifts of the extratropical jet stream in response to global warming. *Journal of Climate*, *29*(23), 8399–8421. https://doi.org/10.1175/JCLI-D-16-0140.1

Watanabe, M. (2005). On the presence of annular variability in an aquaplanet model. *Geophysical Research Letters*, *32*, L05701. https://doi.org/10.1029/2004GL021869

Wing, A. A., Reed, K. A., Satoh, M., Stevens, B., Bony, S., & Ohno, T. (2018). Radiative–convective equilibrium model intercomparison project. *Geoscientific Model Development*, *11*(2), 793–813. https://doi.org/10.5194/gmd-11-793-2018

Yin, J. H. (2005). A consistent poleward shift of the storm tracks in simulations of 21st century climate. *Geophysical Research Letters*, *32*, L18701. https://doi.org/10.1029/2005GL023684

Zappa, G., Lucarini, V., & Navarra, A. (2011). Baroclinic stationary waves in aquaplanet models. *Journal of the Atmospheric Sciences*, *68*(5), 1023–1040. https://doi.org/10.1175/2011JAS3573.1